Quantifying the contribution of dust to alpine soils in the periglacial zone of the Uinta Mountains, Utah, USA

Jeffrey S. Munroe[a,*], Emmet D. Norris[a], Pratt M. Olson[a], Peter C. Ryan[a], Michael J. Tappa[b], Brian L. Beard[b]

[a] Geology Department, Middlebury College, 276 Bicentennial Way, Middlebury, VT 05753, USA
[b] Department of Geosciences, University of Wisconsin-Madison, 1215 W. Dayton St., Madison, WI 53706, USA

ABSTRACT

Profiles of alpine soils in the Uinta Mountains (Utah, USA) were investigated to determine how long-term dust deposition has influenced soil properties in this environment. Field studies were focused on four above-treeline sites, all of which were apparently beyond the reach of erosive glacial ice during the Pleistocene. Modern dust, soil A and B horizons, and local bedrock were compared in terms of major and trace element geochemistry, along with Sr and Nd isotope compositions. In all cases, soil samples are a mixture of dust and local bedrock end members, with A horizons more closely resembling dust, and B horizons more similar to bedrock. Calculations estimate that these soil profiles contain ~50 to 80% dust, which is effectively mixed downward into the solum by cryoturbation. Because these landscape positions were not glaciated, the total amount of dust contained within soil profiles is large relative to sites at lower elevation within the glacial limit. In addition to altering physical properties of these soil profiles, including horizonation and texture, deposition of dust rich in base cations positively influences soil fertility.

1. Introduction

In the classic open-system model of soil formation, pedogenesis occurs in response to inputs to, and outputs from, the soil system, along with translocations and transformations within the soil profile (Huggett, 1975). In desert environments, considerable research has established that the deposition of eolian sediment to the soil surface in the form of mineral dust is a significant input guiding pedogenesis (e.g. Reheis, 1999; Reheis and Kihl, 1995; Yaalon and Ganor, 1973). Similar work has demonstrated that eolian inputs can also exert an important control on the mineralogy and chemistry of tropical soils (e.g. Dia et al., 2006; Dymond et al., 1974; Kurtz et al., 2001; Li et al., 2016). A more recent realization is the role played by dust additions to soils in mountain ecosystems (e.g. Dahms, 1993; Gild et al., 2018; Johnston, 2001; Küfmann, 2003; Lawrence et al., 2013; McGowan et al., 2005). In the western United States in particular, studies have documented pedologic and stratigraphic evidence for past dust deposition (e.g. Birkeland et al., 1987; Litaor, 1987; Muhs and Benedict, 2006; Thorn and Darmody, 1980). Some projects have attempted to quantify rates of contemporary dust accumulation (e.g. Dahms and Rawlins, 1996; Lawrence et al., 2010; Munroe, 2014), and to identify possible dust

source regions (e.g. Muhs and Benedict, 2006; Munroe et al., 2019). Still other studies have investigated the cumulative effects of dust deposition on soil chemistry and fertility (e.g. Aciego et al., 2017; Lawrence et al., 2013, Lawrence et al., 2011). Collectively this work has illuminated the crucial role that dust deposition plays in the form and functioning of the mountain "critical zone", defined as the "*dynamic interface between the solid Earth and its fluid envelopes*" (National Research Council, 2001).

Despite this clear and growing recognition of the role of dust as an input to mountain soil formation, many questions remain unanswered. For instance, given a paucity of direct measurements, understanding of how dust deposition rates vary geographically is incomplete (e.g. Lawrence and Neff, 2009). Information about changes in dust deposition rates over time is even sparser (e.g. Arcusa et al., 2019; Heindel et al., 2020; Neff et al., 2008; Routson et al., 2019, Routson et al., 2016). It is clear from some studies that dust can comprise a substantial fraction of the parent material for mountain soils (e.g. Aciego et al., 2017; Lawrence et al., 2011), but this situation has only been investigated in a few settings for soils formed over a restricted range of lithologies. Furthermore, studies of soils in high mountain environments have tended to focus on landscape positions that were glaciated

---

during the Pleistocene (e.g. Küfmann, 2003; Lawrence et al., 2013). Soils in these areas, therefore, post-date the last deglaciation and are < 20,000 years old (Clark et al., 2009). As a result, the effects of dust deposition on alpine soil formation over longer timescales in periglacial settings are unknown.

Here we investigate the role of long-term dust deposition in the formation of alpine soils on a periglacial upland in the Rocky Mountains that was not subjected to Pleistocene glaciation. These soils have likely formed over timescales of > 10^6 years under the influence of varying climatic conditions. Samples of modern dust, soil A and B horizons, and bedrock collected from 4 different sites were analyzed for a suite of physical and chemical properties. Results were used to estimate the average fraction of modern soil profiles comprised of exogenous dust and to identify the effects of long-term dust deposition on alpine pedogenesis.

2. Setting and methods

2.1. Physical setting

Fieldwork for this project was conducted in the Uinta Mountains (hereafter, the "Uintas"), a prominent subrange of the Rocky Mountain System located in northeastern Utah, USA (Fig. 1). The Uintas, which have maximum summit elevations > 4 km, were uplifted in the early Cenozoic Era as tectonic convergence along the west coast of North America drove the Laramide Orogeny (Bradley, 1995; Sears et al., 1982). The bedrock of the Uintas is a several-km-thick sequence of siliciclastic sedimentary rocks including argillite, sandstone, and conglomerate (Condie et al., 2001; Dehler et al., 2007). The most resistant layers in this stratigraphy are the sandstones, ranging from quartz arenite to arkose, some of which have been metamorphosed to quartzite. The Uintas were extensively glaciated at times during Pleistocene, as illustrated by their well-developed alpine glacial geomorphology (Laabs and Carson, 2005; Munroe, 2005). During the peak of the last glaciation, ca. 20,000 years ago, the range hosted > 2000 km^2 of flowing glacial ice (Laabs et al., 2009; Munroe and Laabs, 2009). In the central and eastern part of the Uintas, these glaciers were mostly confined to discrete valleys and only locally overtopped adjacent interfluves. As a result, the highest elevations of the Uintas are a periglacial landscape that was beyond the reach of the erosive Pleistocene valley glaciers. Today the landscape above treeline (> 3100 m) is a mosaic of exposed rock, semi-perennial snowfields, periglacial patterned-ground, and gently sloping, tundra-mantled alpine soils that are the subject of this investigation.

Climatic conditions in the alpine zone of the Uinta Mountains are constrained by the Chepeta remote automated weather station (RAWS), located at an elevation of 3694 m and central to the study sites for this project (Fig. 1). This RAWS recorded a mean temperature of −2.0 °C between January 1, 2000 and December, 31, 2019 (n = 6644 observations). Annual precipitation, as estimated by PRISM data, averages ~ 900 mm ("PRISM Climate Group, Oregon State U," n.d.), much of which falls as snow.

2.2. Fieldwork

Fieldwork for this project focused on collection of three types of material for use in elucidating the contribution of dust to alpine soils: dust, soil, and bedrock. Contemporary dust samples have been collected at locations throughout the alpine zone of the Uintas since 2011 (Munroe, 2014). Dust is collected in passive samplers that are a variation of the classic marble dust trap (Reheis and Kihl, 1995; Sow et al., 2006; Wesely and Hicks, 2000) altered for use in a high-precipitation environment. Briefly, each sampler features a clear polycarbonate tray measuring 56 × 56 cm by 7.5 cm deep. The trays are divided into 5 troughs with a V-shaped cross-section, each of which is filled with 1.75-cm diameter glass beads (~7 kg per sampler). The beads form a rough

surface that traps dust from the air, protects previously deposited dust from the wind, and greatly reduces the possibility of dust splashing out during precipitation events. The troughs inevitably collect water as well as dust, but the black beads allow for solar heating to evaporate water between precipitation events. If the troughs completely fill, a row of small (3 mm) holes at the rim of each trough allows water to trickle out. Dust trapped by the beads settles to the base of each trough where it remains as water evaporates (or overflows). Dust is removed from the sampler by washing the beads and troughs with distilled water (Munroe, 2014; Munroe et al., 2019, Munroe et al., 2015).

There are currently 8 passive dust samplers deployed throughout the Uinta Mountains. Four of these in the eastern part of the Uintas were utilized in this project: Dust-1, Dust-5, Dust-7, and Dust-8 (Fig. 1). These four were selected because they are located in relatively flat areas surrounded by alpine tundra vegetation overlying well-developed soils. Previous studies of soil profiles in this region also provide context for the results generated by this project (Bockheim et al., 2000; Bockheim and Koerner, 1997; Munroe, 2007; Munroe et al., 2015).

Soil samples were collected in two types of hand excavations in the near vicinity (< 100-m radius) of the dust samplers (Fig. 1). First, at three sites a full profile was examined from the surface down to relatively unaltered material (~70–100 cm). These profiles were described following standard methodologies, and samples were collected from each identified horizon. In combination with previously published work on Uinta alpine soils, these pedon descriptions contextualize the degree of development of the soils surrounding each dust sampler. Second, at multiple sites around each dust sampler, shallow hand excavations were made and a representative sample was taken from the A horizon and the B horizon of the soil profile. This strategy provided information about soil pedons in the four study areas, maximized the number of samples available for analysis, and utilized field time effectively in this difficult-to-access region. Soil sampling locations were selected on broad ridge crests and flat landscape positions to minimize the chance that soil profiles were influenced by solifluction. Samples were collected in Whirl-Pak bags, and the location of each site was recorded in a handheld GPS.

Representative samples of quartz arenite and quartzite bedrock were gathered from the ground surface in the vicinity of each dust sampler. These were presumably uplifted from the (otherwise inaccessible) bedrock beneath the regolith and soil mantle by periglacial processes.

A total of 17 dust samples were collected between 2011 and 2019 at the study sites considered in this project (Dust-1, Dust-5, Dust-7, and Dust-8, Fig. 1). During fieldwork, 24 paired samples of soil A and B horizons were collected from the vicinity of these dust samplers: 4 pairs near Dust-1, 8 pairs near Dust-5, 3 pairs near Dust-7, and 9 pairs near Dust-8 (Fig. 1, Table 1). Full soil profiles were described and sampled at Dust-1, Dust-7, and Dust-8 (Table 2); the soil at Dust-5 was too rocky, and despite considerable effort, it was not possible to excavate a deep soil pit at this location (Fig. 1). All together, 58 soil samples, and 15 rock samples, were collected.

2.3. Labwork

Samples of modern dust, soil, and local bedrock from each of the study sites were subjected to an array of laboratory analyses to constrain their physical and chemical properties. Prior to analysis, the fine fraction of soil samples was isolated by sieving to 2-mm after drying for 24 h at 60 °C. Organic matter was removed from dust and soil samples with 35% H_2O_2 over 7 days. Rock samples were crushed for 1 min in a shatterbox to produce a uniform fine powder.

2.3.1. Grain size analysis

The grain size distribution of the dust and fine fraction of the soil samples was investigated by laser scattering in a Horiba LA-950. Samples were dispersed in 3% sodium hexametaphosphate for 1 week,
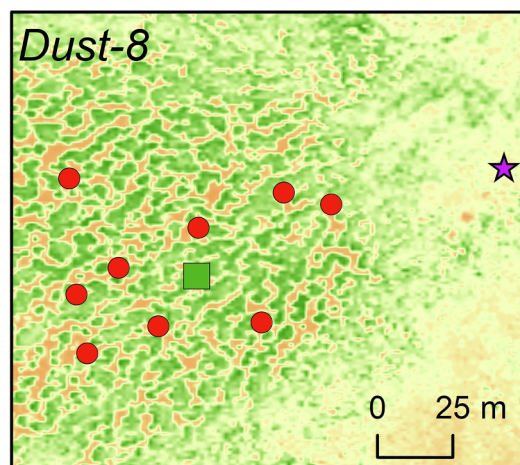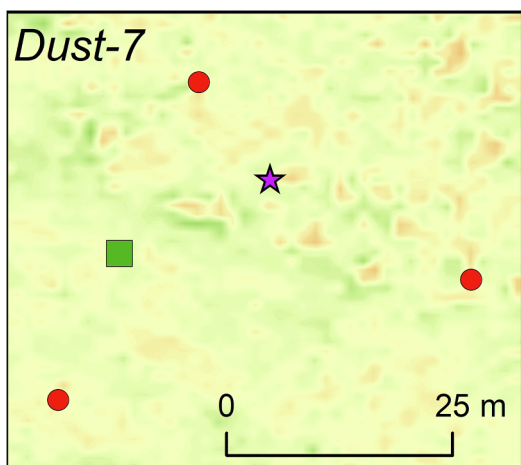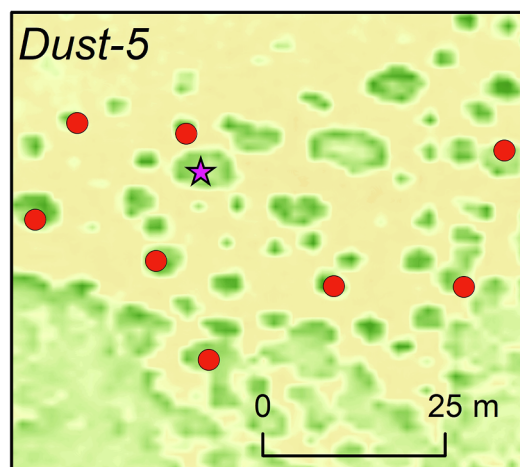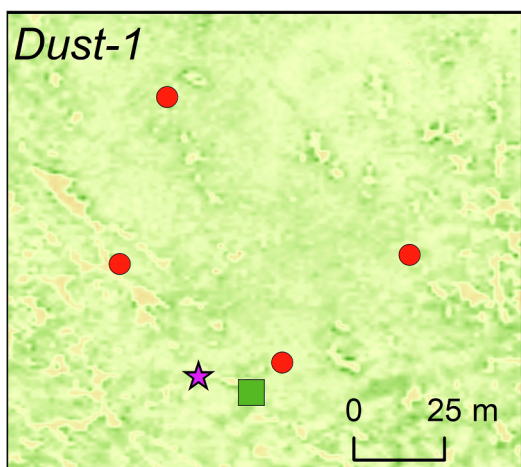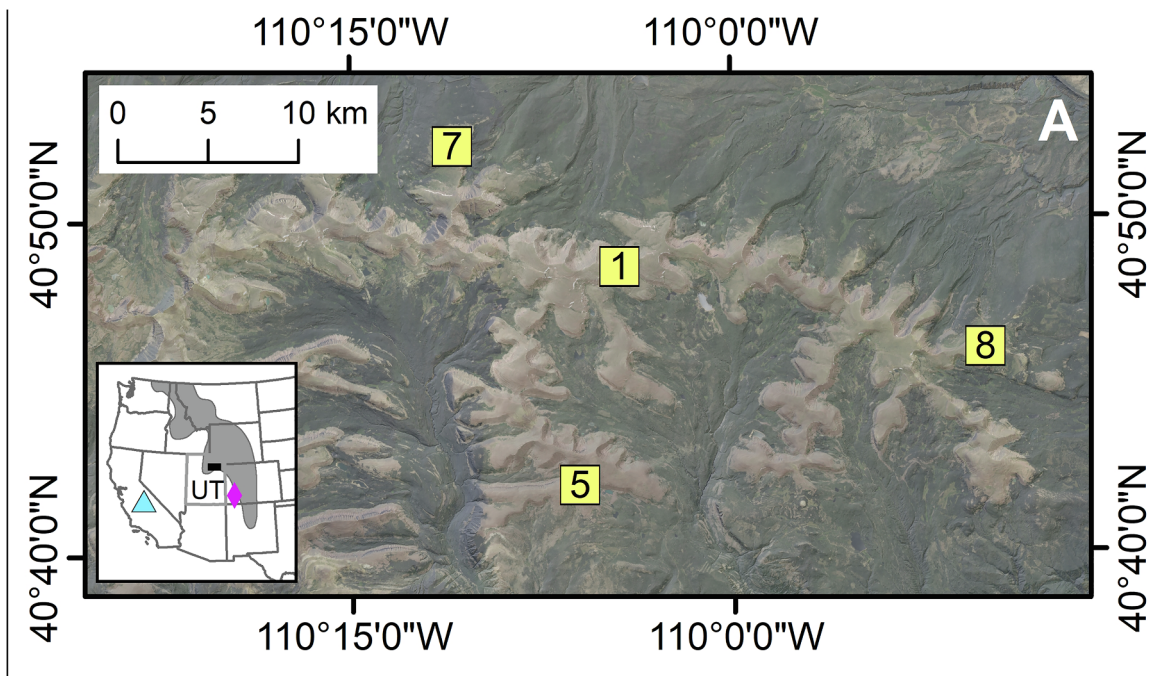
(caption on next page)

Fig. 1. Location map of the study area in the Uinta Mountains. Inset shows the location of the Uinta Mountains (black box) in northeastern Utah (UT). The gray polygon delineates the Rocky Mountain province in the western United States. The blue triangle denotes the location of the Sierra Nevada study (Aciego et al., 2017) and the purple diamond marks the location of the San Juan Mountain study (Lawrence et al., 2011) mentioned in the discussion. Larger figure shows a true color image of the eastern Uinta Mountains with the four study areas identified (Dust-1, Dust-5, Dust-7, and Dust-8). The Chepeta weather station is located at the Dust-1 site. Lower figures present enlargements of these four study areas with site-specific scale bars. The background image in each is a 1-m normalized differential vegetation index (NDVI) to highlight the nature of the periglacial patterned ground at these sites. Greener colors represent more vegetation; orange colors indicate more bare rock. The passive dust samplers are represented by purple stars. Green squares mark the locations of the described soil profile (at Dust-1, Dust-7, and Dust-8). Red circles denote sites of paired A and B horizon samples.

Table 1
Locations, Moisture Content, Organic Content, and Grain Size Distribution of Soil Samples.

Sample Name	Location	Latitude	Longitude	Elevation	Horizon	Moisture	Organic Matter	Mean Size	Median Size	Sand	Silt	Clay	(Clay/Sand)	(Silt + Clay)/Sand
–	–	D.dddddd	D.dddddd	m	–	%	%	µm	µm	%	%	%	–	–
Dust-1-A*	Dust-1	40.809955	−110.073329	3691	A	5.4	8.7	41.2	17.4	19	70	11.1	0.6	4.3
Dust-1-2Bw*	Dust-1	40.809955	−110.073329	3691	2Bwjj	0.8	1.2	34.8	11.5	14.1	81	5.19	0.4	6.1
Dust-1-2Bt*	Dust-1	40.809955	−110.073329	3691	2Btjj	0.5	0.8	50.4	10.6	21.7	72	5.92	0.3	3.6
Dust-1-2BC*	Dust-1	40.809955	−110.073329	3691	2BCjj	1.5	1.7	34.3	9.9	14.5	76	9.39	0.6	5.9
1-E-top	Dust-1	40.810298	−110.072935	3691	A	12.9	10.2	124.8	38.4	42.7	52.6	4.7	0.1	1.3
1-E-bottom	Dust-1	40.810298	−110.072935	3691	B	10.6	2.5	112.7	19.2	37.2	46.8	16.0	0.4	1.7
1-N-top	Dust-1	40.810691	−110.073538	3691	A	9.0	7.5	162.8	116.0	56.2	36.9	6.9	0.1	0.8
1-N-bottom	Dust-1	40.810691	−110.073538	3691	B	7.8	2.6	127.7	25.5	41.3	45.5	13.1	0.3	1.4
1-S-top	Dust-1	40.810030	−110.073252	3691	A	8.5	5.9	150.0	79.5	53.1	39.3	7.6	0.1	0.9
1-S-bottom	Dust-1	40.810030	−110.073252	3691	B	5.8	2.1	160.1	64.1	50.1	39.2	10.7	0.2	1.0
1-W-top	Dust-1	40.810275	−110.073656	3692	A	12.1	7.0	186.6	164.3	62.5	31.6	5.9	0.1	0.6
1-W-bottom	Dust-1	40.810275	−110.073656	3692	B	6.1	1.3	128.9	49.0	46.8	49.3	3.9	0.1	1.1
Dust-5–1 T	Dust-5	40.701072	−110.100432	3591	A	5.4	28.3	19.2	10.2	5.0	81.9	13.1	2.6	19.1
Dust-5-1B	Dust-5	40.701072	−110.100432	3591	B	1.3	5.7	44.9	14.7	21.0	62.1	16.9	0.8	3.8
Dust-5–2 T	Dust-5	40.700905	−110.100642	3592	A	3.1	11.6	32.8	11.3	13.1	71.4	15.6	1.2	6.7
Dust-5-2B	Dust-5	40.700905	−110.100642	3592	B	3.4	15.3	28.8	12.9	12.1	71.2	16.7	1.4	7.3
Dust-5–3 T	Dust-5	40.700814	−110.100796	3592	A	4.2	19.4	20.9	8.5	7.8	73.5	18.7	2.4	11.8
Dust-5-3B	Dust-5	40.700814	−110.100796	3592	B	2.0	5.8	25.2	9.6	9.8	72.5	17.7	1.8	9.2
Dust-5–4 T	Dust-5	40.701106	−110.100958	3593	A	5.9	30.7	19.9	11.0	5.9	84.0	10.1	1.7	15.9
Dust-5-4B	Dust-5	40.701106	−110.100958	3593	B	1.2	2.7	24.9	10.9	10.6	83.3	6.1	0.6	8.4
Dust-5–5 T	Dust-5	40.700987	−110.101010	3593	A	4.2	20.5	22.3	11.1	7.9	77.9	14.3	1.8	11.7
Dust-5-5B	Dust-5	40.700987	−110.101010	3593	B	1.0	2.4	19.2	8.8	5.8	89.9	4.3	0.8	16.4
Dust-5–6 T	Dust-5	40.700936	−110.100861	3592	A	4.8	21.2	17.4	7.9	5.4	75.9	18.7	3.5	17.6
Dust-5-6B	Dust-5	40.700936	−110.100861	3592	B	0.5	1.8	128.1	109.0	55.7	33.6	10.7	0.2	0.8
Dust-5–7 T	Dust-5	40.700904	−110.100482	3591	A	4.7	23.3	24.9	13.3	9.3	76.6	14.1	1.5	9.7
Dust-5-7B	Dust-5	40.700904	−110.100482	3591	B	2.1	6.4	24.6	9.9	9.5	76.3	14.1	1.5	9.5
Dust-5–8 T	Dust-5	40.701093	−110.100824	3592	A	5.8	31.6	34.6	14.2	13.4	76.1	10.5	0.8	6.5
Dust-5-8B	Dust-5	40.701093	−110.100824	3592	B	1.8	6.8	21.6	8.0	8.5	80.1	11.4	1.3	10.8
Dust-7-AT*	Dust-7	40.870616	−110.182708	3589	A	2.4	11.2	22.0	10.5	8.1	72.7	19.2	2.4	11.4
Dust-7-AB*	Dust-7	40.870616	−110.182708	3589	2Bwjj	2.7	5.6	12.2	7.3	1.3	80.1	18.6	14.8	78.4
Dust-7-BT	Dust-7	40.870470	−110.182769	3589	A	2.1	7.6	21.1	10.8	6.9	75.5	17.6	2.5	13.4
Dust-7-BB	Dust-7	40.870470	−110.182769	3589	B	0.5	1.4	206.4	33.3	43.8	47.7	8.4	0.2	1.3
Dust-7-CT	Dust-7	40.870590	−110.182358	3590	A	1.7	8.7	34.2	15.5	15.2	72.7	12.1	0.8	5.6
Dust-7-CB	Dust-7	40.870590	−110.182358	3590	B	0.8	3.6	87.3	33.1	37.4	53.9	8.7	0.2	1.7
Dust-7-DT	Dust-7	40.870787	−110.182629	3589	A	2.5	9.0	17.4	7.4	5.5	75.1	19.5	3.6	17.3
Dust-7-DB	Dust-7	40.870787	−110.182629	3589	B	0.8	2.1	42.0	11.6	16.6	67.1	16.3	1.0	5.0
Dust-8-A*	Dust-8	40.768058	−109.835042	3663	A	13.3	22.7	15.3	6.7	4.3	71.9	23.7	5.5	22.1
Dust-8-2Bw*	Dust-8	40.768058	−109.835042	3663	2Bwjj	1.3	3.1	36.8	13.8	16.2	72.8	11.0	0.7	5.2
Dust-8-2Bt*	Dust-8	40.768058	−109.835042	3663	2Btjj	1.1	1.8	46.5	21.7	23.1	70.4	6.5	0.3	3.3
Dust-8-2BC*	Dust-8	40.768058	−109.835042	3663	2BCjj	1.4	1.9	40.3	13.3	19.9	65.0	15.1	0.8	4.0
Dust-8-BT	Dust-8	40.768203	−109.835036	3664	A	12.9	39.8	25.1	13.2	9.1	77.7	13.2	1.4	10.0
Dust-8-BB	Dust-8	40.768203	−109.835036	3664	B	2.2	6.4	26.7	13.0	10.9	76.9	12.1	1.1	8.1
Dust-8-CT	Dust-8	40.767909	−109.835156	3662	A	6.4	31.0	29.1	15.0	11.6	76.3	12.2	1.1	7.6
Dust-8-CB	Dust-8	40.767909	−109.835156	3662	B	2.0	6.5	26.0	12.9	10.5	78.0	11.5	1.1	8.5
Dust-8-DT	Dust-8	40.767828	−109.835369	3660	A	7.3	38.7	25.8	13.2	9.9	76.3	13.9	1.4	9.1
Dust-8-DB	Dust-8	40.767828	−109.835369	3660	B	1.8	5.9	26.1	11.0	10.4	78.0	11.6	1.1	8.7
Dust-8-ET	Dust-8	40.768351	−109.835422	3662	A	5.3	26.9	20.9	8.1	7.2	71.5	21.3	3.0	12.9
Dust-8-EB	Dust-8	40.768351	−109.835422	3662	B	1.5	6.0	37.5	13.6	17.2	67.1	15.7	0.9	4.8
Dust-8-FT	Dust-8	40.768084	−109.835275	3662	A	2.7	10.1	25.4	14.1	9.4	79.1	11.5	1.2	9.6
Dust-8-FB	Dust-8	40.768084	−109.835275	3662	B	1.2	4.0	50.9	19.0	24.1	65.4	10.5	0.4	3.1
Dust-8-GT	Dust-8	40.768308	−109.834782	3665	A	5.3	26.1	28.4	12.7	10.2	75.8	14.0	1.4	8.8
Dust-8-GB	Dust-8	40.768308	−109.834782	3665	B	1.9	4.3	26.4	11.3	10.1	77.8	12.1	1.2	8.9
Dust-8-HT	Dust-8	40.768273	−109.834640	3666	A	2.2	9.3	31.1	13.6	12.7	77.6	9.6	0.8	6.9
Dust-8-HB	Dust-8	40.768273	−109.834640	3666	B	1.6	5.7	36.8	14.8	15.9	78.6	5.5	0.3	5.3
Dust-8-IT	Dust-8	40.768004	−109.835401	3661	A	7.5	28.2	18.8	7.0	5.2	72.2	22.7	4.4	18.3
Dust-8-IB	Dust-8	40.768004	−109.835401	3661	B	1.7	3.6	31.5	14.7	13.7	73.8	12.5	0.9	6.3
Dust-8-JT	Dust-8	40.767920	−109.834848	3664	A	6.3	31.3	21.3	9.7	7.4	76.1	16.4	2.2	12.4
Dust-8-JB	Dust-8	40.767920	−109.834848	3664	B	2.3	8.9	34.3	13.0	14.7	69.3	16.0	1.1	5.8

*Samples from full profile.

Table 2
Field Descriptions of Soil Profiles.

Site –	Horizon –	Depth* cm	Thickness** cm	Boundary –	Color –	Texture –	Primary Structure	Secondary Structure	Moist Consistence	Wet Consistence	Roots –	Stones %	Cobbles %	Gravel %
Dust-1	A	0–28	28–70	AI	7.5YR 2.5/2	Si 5%	cbk	fgr	mvfr	so/ps	2mf	5	10	10
Dust-1	2Bwjj	28–60	5–30	CI	5YR 4/4	S 5%	mgr	fgr	mvfr	so/po	1fvf	10	10	25
Dust-1	2Btjj	60–85	25	CI	5YR 4/4	LS 10%	fsbk	fgr	mfr	so/po	–	20	15	20
Dust-1	2BCjj	85–92 +	7+	–	5YR 4/6	SL 5%	sg	–	mvfr	so/po	–	20	10	10
Dust-7	A	0–15	15	AI	7.5YR 2.5/2	Si 5%	fgr	–	mvfr	ss/po	3f, vf 2 m	10	10	5
Dust-7	2Bwjj	15–67 +	52+	–	5YR 4/4	SL 5%	fpl	–	mfr	so/po	1co, m, f	25	15	10
Dust-8	A	0–12	10–23	CW	10YR 2.5/1	Si 5%	fgr	–	mfr	ss/po	3f, vf 2 m	5–10	5	20
Dust-8	2Bwjj	12–37	25–30	CW	5YR 4/4	S 0%	fpl	sg	mvfr	so/po	1co, m, f	25	15	25
Dust-8	2Btjj	37–60	20–25	CW	5YR 4/3	SiL 10%	fpl	mgr	mfi	ss/ps	1co, m, f	20	10	10
Dust-8	2BCjj	60–70 +	10+	–	5YR 4/6	SL 5%	fsbk	vfsbk	mvfr	ss/ps	–	20	10	10

*Depth below ground surface in described section.
**Range in thickness across the width of the excavated pit (~100 cm).
Boundary: AI, abrupt irregular; CI clear irregular; CW, clear wavy.
Texture: Si, silt; S, sand; LS, loamy sand; SL, sandy loam; SiL, silt loam.
Structure: Ped size – c, coarse; m, medium; f, fine; vf, very fine.
Structure: Ped shape – bk, blocky; gr, granular; sbk, subangular blocky; pl, platy; sg, single grain.
Consistence: mvfi, very firm; mfr, friable; mfi, firm; so, nonsticky; ss, slightly sticky; po, nonplastic; ps, slightly plastic.
Roots: 1, few; 2, common, 3, many; vf, very fine; f, fine; m, medium; co, coarse.

and mechanically mixed and sonified immediately before analysis. The LA-950 has an effective range from 10 nm to 3 mm, and a refractive index of 1.54 with an imaginary component of 0.1i was used in calculating the grain size distribution. The abundance of particle size classes was determined from the cumulative distribution curve as: coarse sand, > 500 μm; medium sand, 500–250 μm; fine sand, 250–125 μm; very fine sand, 125–63 μm; coarse silt, 63–30 μm; medium silt, 30–14 μm; fine silt, 14–7 μm; very fine silt, 7–2 μm; clay < 2 μm.

2.3.2. Loss-on-Ignition

Soil samples were subjected to sequential loss-on-ignition (LOI) analysis in a Leco TGA-701 thermogravimetric analyzer. Samples (~5 g) were first heated to 105 °C for 3 h under a N_2 atmosphere to calculate moisture content. Next, the temperature was increased to 550 °C under an ambient atmosphere for 4 h to determine mass loss as a proxy for organic matter content (Dean, 1974).

2.3.3. Geochemistry

Determination of major and trace element abundances in dust, soil, and rock samples was conducted with a combination of X-ray fluorescence (XRF) and Inductively-Coupled Plasma Mass Spectrometry (ICP-MS). In preparation for analysis, samples of soil and powdered rock were ignited at 1000°C in a Leco TGA-701 thermogravimetric analyzer. After ignition, soil samples along with some rock samples were ground with a mortar and pestle and then added to a borate flux (66.67% $Li_2B_4O_7$ – 32.83% $LiBO_2$ – 0.50% LiI) in a platinum crucible. This mixture was then heated to 1065 °C for 20 min in a Le Neo Fluxer to produce a glass disk that was analyzed for major and some trace elements on a Thermo ARL Quant'X EDXRF. Results were calibrated with the USGS Glass Mountain Rhyolite (RGM-1) standard, along with in-house standards constructed from NIST materials, all of which were made into glass disks in the same manner as samples.

Major and trace element abundances in dust samples, along with some rock samples, were determined through ICP-MS analysis. Some dust samples were analyzed at Middlebury College on a Thermo iCapQ ICP-MS after lithium metaborate fusion and dissolution in trace-element grade nitric acid. Other samples were analyzed at SGS Minerals following methods GE-ICP91A50 and GE-ICM40B after multi-acid digestion and fusion.

Major element abundances results reported by the XRF in the form of weight percent oxide were converted to atomic (elemental) abundances for comparison with results generated by ICP-MS analysis. To avoid the diluting effect of quartz that is the major mineral in the Uinta lithologies, major element abundances were normalized to Fe (Reheis et al., 2002). For the 10 elements measured in all dust, soil, and rock samples (Na, Mg, Al, K, Ca, Ti, Fe, Rb, Sr, and Zr) a principle component analysis was conducted using a varimax rotation and an eigenvalue extraction threshold of 1. This process simplified the full geochemical dataset to the minimum number of components necessary to summarize the variability in major and trace element abundances.

2.3.4. Sr and Nd isotopes

Representative dust, soil, and rock samples were analyzed for their Sr and Nd isotope values in the ICP-TIMS Isotope Laboratory at the University of Wisconsin-Madison. Eighteen samples of dust and rock analyzed in February 2020 were added to existing results (Munroe et al., 2019) to produce a comprehensive dataset on Sr and Nd variability in Uinta dust, soils, and rock. A detailed methodology for these analyses was presented in prior work (Munroe et al., 2019) and the data reported in this study were generated following the same methods. Strontium was analyzed by Thermal Ionization Mass Spectrometry with exponential normalization to an $^{86}Sr/^{88}Sr = 0.1194$, and Nd was analyzed by multi collector inductively coupled plasma mass spectrometry with exponential normalization to a constant $^{146}Nd/^{144}Nd$ of 0.7219. During the course of this study, the average $^{87}Sr/^{86}Sr$ for SRM-987 was 0.710275 ± 0.000020 (2σ; n = 20) and for the USGS N-1 standard the average $^{87}Sr/^{86}Sr$ was 0.709198 ± 0.000006 (2σ; n = 6). For Nd isotopes the average $^{143}Nd/^{144}Nd$ for JNdi-1 was 0.512114 ± 0.000010 (2σ; n = 16) and for the in-house UW Ames I standard the average $^{143}Nd/^{144}Nd$ was 0.512146 ± 0.000014 (2σ; n = 10). The isotope ratios measured for the standards in this study agree with the isotope ratios reported for these standards in Munroe et al. (2019); no inter-laboratory corrections were applied.

2.3.5. Mixing model

Given their setting, alpine soils of the Uintas can reasonably be modeled as a mixture of two different mineral parent materials, dust (D) and local bedrock (R), which can be treated as endmembers. With this starting assumption, the following mixing model (Colville et al., 2011; Faure, 1997) was employed to determine the fraction of dust (f_{dust}) in soil samples:

$$R_m = \frac{f_{dust}\,[C_e]\,(R_{dust}) + f_{rock}\,[C_e]\,(R_{rock})}{f_{dust}\,[C_e] + f_{rock}\,[C_e]}$$

R_m is the value of $^{87}Sr/^{86}Sr$ or $^{143}Nd/^{144}Nd$ (expressed as ε_{Nd})
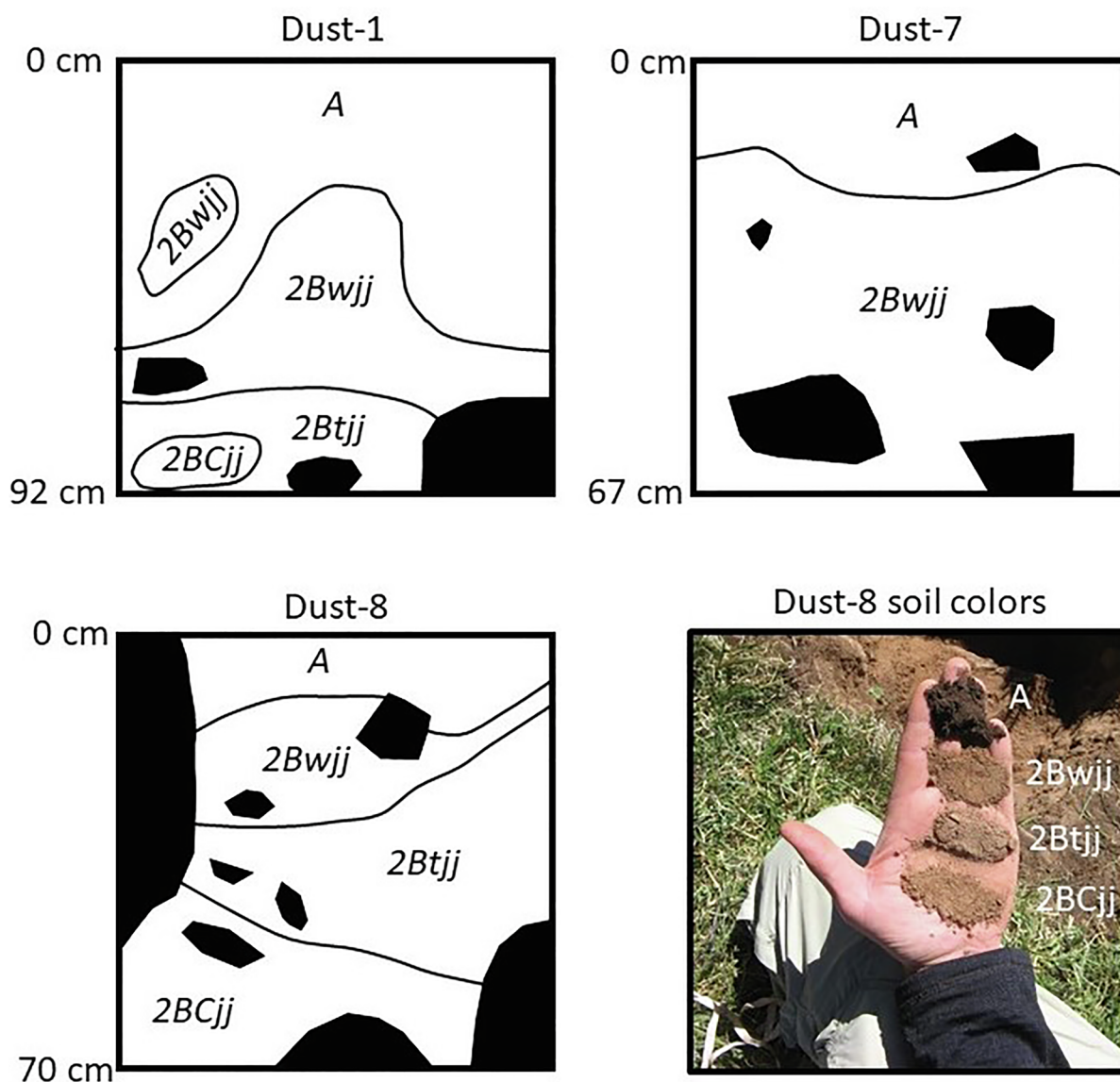
Fig. 2. Sketches of the soil profiles described at Dust-1, Dust-7, and Dust-8. The soil was too rocky for a full-scale excavation at Dust-5. Horizons designations are presented, along with the nature of boundaries, and the locations of larger coarse fragments. No attempt was made to draw the abundant gravel and smaller cobbles. Lower right presents the colors of the four horizons identified in the soil profile at Dust-8. (For interpretation of the references to colour in this figure legend, the reader is referred to the web version of this article.)

calculated for a particular soil sample. C_e is the average concentration of Sr or Nd measured in the dust and rock end members. R_e is the concentration-weighted average value of $^{87}Sr/^{86}Sr$ or ε_{Nd} in the rock and dust end members. The sum of f_{dust} and f_{rock} equals 1, therefore $f_{rock} = (1 - f_{dust})$. The equation was solved for $^{87}Sr/^{86}Sr$ and ε_{Nd} by varying f_{dust} from 0 to 1.0 in steps of 0.01 to yield a mixing line for each element. Values of $^{87}Sr/^{86}Sr$ and ε_{Nd} determined for the soil samples ($\pm 2\sigma$) were then intersected with these mixing lines to determine the range of dust fractions in the soils.

3. Results

The full soil profiles described and sampled at Dust-1, Dust-7, and Dust-8 exhibit strong similarity with one another, along with abundant evidence for cryoturbation (Fig. 2, Table 2). Each profile contains a dark black A horizon (7.5YR 2.5/2 or 10YR 2.5/1) from 10 to 20 cm thick that exhibits granular structure and a relatively low abundance of coarse fragments. In all profiles this A horizon transitions across an irregular boundary to a 2Bwjj horizon with a redder color of 5YR 4/4.

Platy structure is clearly visible in this horizon in the profile at Dust-7 and Dust-8. This horizon also exhibits the impact of profound cryoturbation at Dust-1, where a tongue of B horizon material appears to rise toward the surface, flanked by downwarped sections of A horizon (Fig. 2). An isolated pocket of 2Bwjj material was also observed within the A horizon. Such evidence for cryoturbation is consistent with the well-developed sorted stone polygons present in all of these sites, and the strong periglacial climate.

Deeper in the profiles at Dust-1 and Dust-8, a 2Btjj horizon was encountered (Fig. 2, Table 2). Clay contents in this material are greater than in the overlying cambic horizon, and evidence for translocation of silt (in the form of silt caps on clasts) and clay (as cutans and clay bridges) was noted. A wavy lower boundary for this horizon at both Dust-1 and at Dust-8 is further evidence of cryoturbation at depths > 50 cm.

The profiles at Dust-1 and Dust-8 reached a 2BCjj horizon where the clay and silt content decreased again and structure trended toward very fine subangular blocky and single grain (Fig. 2, Table 2). Similarly unaltered material was not encountered in the excavation at Dust-7,
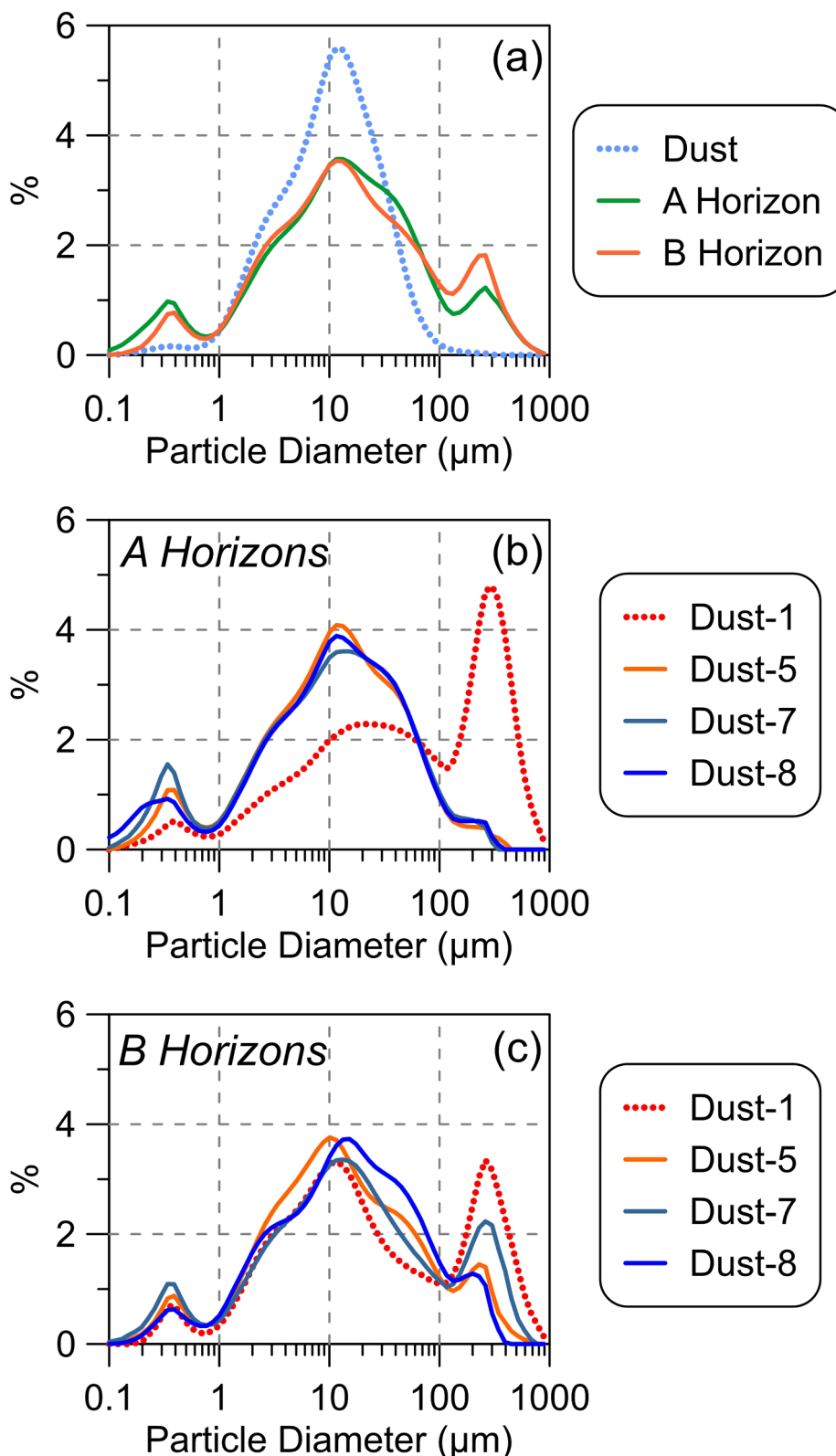
Fig. 3. Grain size distributions for dust and soils determined by laser scattering. (a) Average grain size distribution for dust (n = 51), A horizon (n = 27), and B horizon (n = 31) samples. (b) Average A horizon and (c) average B horizon size distributions for each of the four sites. All samples have a prominent mode ~ 10–15 μm. Soil horizons also contain a mode in the sand range; this is notably elevated in the A horizons at Dust-1 (dotted line), as discussed in the text.

although the distinction with the 2Bwjj and 2Btjj horizons is subtle, so 2BCjj material may have been missed at this site.

Grain size distributions reveal similarities, but also clear differences between dust and soil sample types. Dust samples collected across the Uintas between 2011 and 2019 (n = 51) are uniformly well-sorted with an average grain size of ~ 15 μm (Fig. 3a). The A and B horizon samples exhibit considerable overlap with one another, reflecting the degree of mixing in these cryoturbated soil profiles. In general, grain size
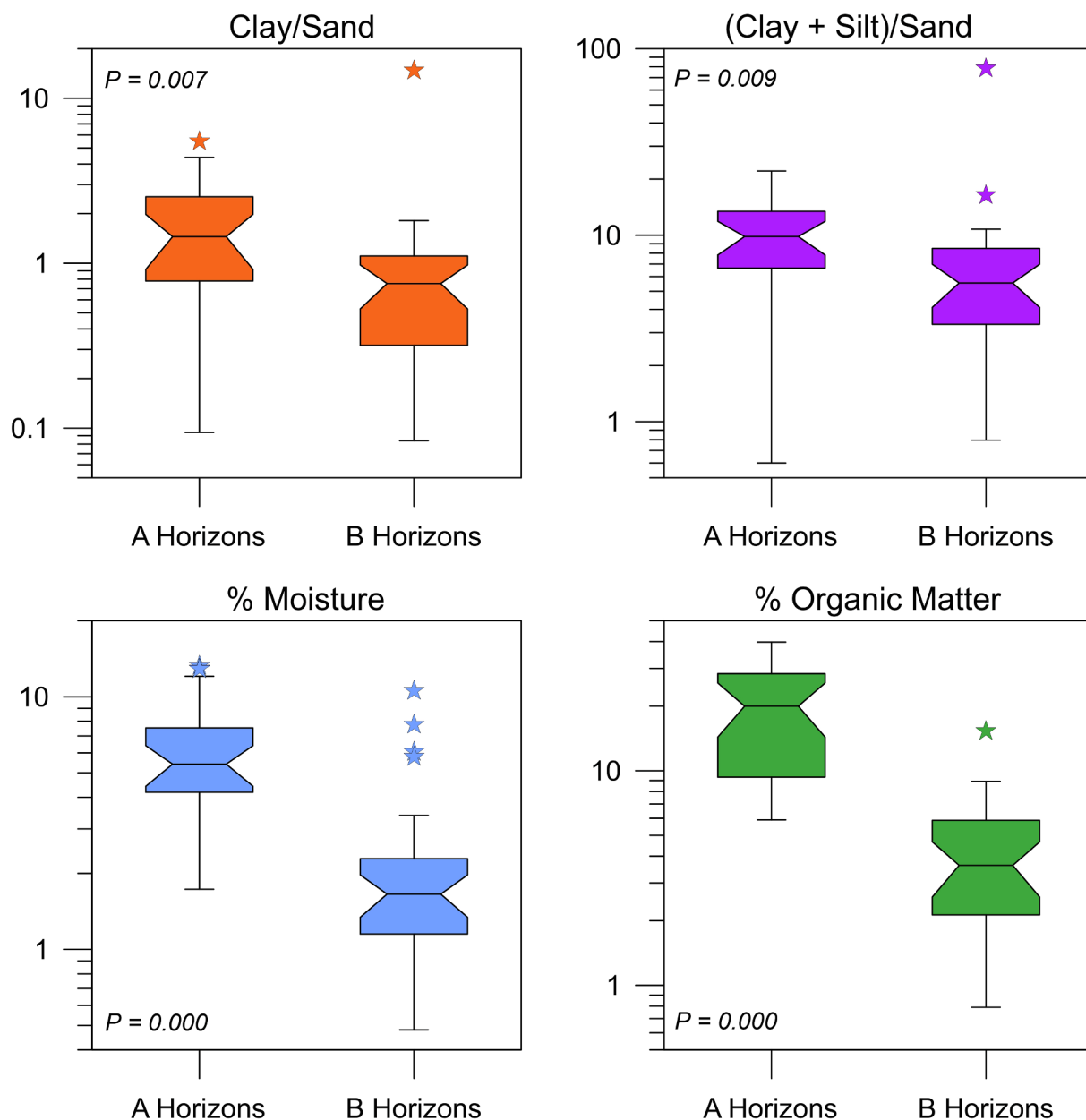
Fig. 4. Boxplots illustrating differences between soil A and B horizons. Central lines represent median values, box represents interquartile range, whiskers represent interquartile range × 1.5, and stars represent outliers. A horizons have significantly higher ratios of Clay/Sand and (Silt + Clay)/Sand compared with B horizons. A horizons also have significantly greater moisture content and organic matter abundance. Note that Y-axes are logarithmic.

distributions of the soil samples are multi-modal, with a prominent mode centered on fine silt (10–15 μm), a minor secondary mode in the fine to coarse sand (150–500 μm) range, and a third mode of submicron material (Fig. 3a).

Individual A-B horizon pairs exhibit a range of patterns; typically the A horizons are finer, but not in all cases (Table 1). Close inspection of the average grain size distributions reveals that B horizons at Dust-5, Dust-7, and Dust-8 are generally coarser than A horizons at these sites (Fig. 3b,c). It is also clear that both types of horizons contain a fine silt peak (~15 μm) matching that of the modern dust (Fig. 3b,c). The Dust-1 site is an outlier, with considerable sand in the A horizon (Fig. 3b). Previous work has presented evidence for redistribution of locally derived, coarse sediment across the ground surface at this site by winter winds (Munroe et al., 2019), which likely explains the prominent spike of coarse material in the average grain size distribution of the surface soil (Fig. 3b).

In general, the abundance of silt alone is not significantly different

between A and B horizons (Table 1). On the other hand, clay-sized material is significantly more abundant in A horizons overall, and sand is significantly more abundant in B horizons. The ratio Clay/Sand, therefore, is strongly contrasting between the two types of horizons (Fig. 4), with a mean of 1.8 in A horizons, and 1.2 in B horizons ($P = 0.007$). The ratio (Clay + Silt)/Sand is similarly contrasting, with a mean of 10.1 in the topsoil and 7.9 in the subsoil ($P = 0.009$).

Loss-on-ignition analysis further reinforces the distinction between A and B horizons in terms of their moisture and organic matter contents (Fig. 4, Table 1). The mean moisture content of A horizons (n = 27) is 6.1%, in contrast to 2.3% for the B horizon samples (n = 31). Similarly, the mean organic matter content of the A horizons, constrained as percent mass loss at 550 °C, is 19.5% in contrast to 4.2% for the B horizons. Both of these differences are highly significant ($P = 0.000$).

The combination of XRF and ICP-MS analysis yielded a comprehensive dataset of geochemical data for these samples (Table 3). The ratios Na/Fe, Mg/Fe, K/Fe, Ti/Fe, Ca/Fe, and Al/Fe all exhibit a clear

Table 3
Major and Trace Element Geochemistry of Dust, Soil, and Rock Samples.

Sample Name	Material	Na %	Mg %	Al %	Si %	P %	K %	Ca %	Ti %	Mn %	Fe %	V ppm	Cr ppm	Cu ppm	Rb ppm	Sr ppm	Zr ppm	Ba ppm	Pb ppm	Th ppm	PC-1	PC-2
Dust-1 < 63 um	Fine Dust	0.86	1.10	7.64	—	0.76	2.51	1.21	0.24	—	2.15	63.00	31.00	166.00	122.00	167.00	40.20	812.00	157.00	12.00	1.28	-0.33
1 < 63um	Fine Dust	0.79	1.09	6.74	—	0.80	2.58	0.89	0.36	—	2.00	62.00	45.00	104.00	113.00	163.00	94.50	641.00	45.40	11.60	0.99	-0.06
DUST1 < 63um	Fine Dust	0.94	0.94	6.81	—	1.35	2.44	1.08	0.29	—	2.11	60.00	43.00	1290.00	109.00	181.00	89.20	757.00	113.00	11.20	1.14	-0.26
1 < 63 um	Fine Dust	0.84	1.01	6.94	—	0.54	2.41	1.02	0.31	—	1.97	62.00	63.00	92.50	107.00	181.00	104.00	632.00	128.00	10.90	1.07	-0.21
Dust-1 Sum 15	Fine Dust	0.96	1.03	7.90	—	—	2.70	0.97	0.46	—	2.09	76.48	102.39	73.97	111.45	198.62	377.86	631.64	26.43	11.29	0.77	0.72
Dust-1 Sum 16	Fine Dust	0.76	0.96	6.76	—	—	2.62	0.57	0.44	—	2.06	69.11	109.14	65.52	114.21	163.57	321.74	542.29	45.57	11.20	0.41	0.68
Dust-5 Sum 16	Fine Dust	1.15	1.21	7.00	—	—	2.75	0.93	0.43	—	2.06	73.81	112.33	71.54	113.08	198.26	233.79	633.15	53.65	12.93	1.19	0.25
Dust-7 Sum 16	Fine Dust	0.82	1.00	6.99	—	—	2.16	1.01	0.43	—	2.61	139.22	142.12	97.44	104.66	214.17	225.37	669.88	62.98	13.15	0.89	0.31
Dust-8 Sum 16	Fine Dust	0.80	0.86	5.27	—	—	1.86	3.40	0.45	—	2.16	81.10	86.79	115.33	80.91	232.83	167.92	642.86	47.82	9.28	1.81	-0.66
Dust-1 Fall 16	Fine Dust	0.96	1.03	6.59	—	—	2.25	0.91	0.40	—	2.12	73.17	117.13	90.52	111.84	214.70	256.16	719.46	56.03	12.32	0.97	0.21
Dust-5 Fall 16	Fine Dust	1.04	1.29	7.46	—	—	2.35	0.92	0.41	—	2.19	80.29	125.03	85.50	114.56	226.04	228.00	735.32	64.76	11.79	1.25	0.20
Dust-7 Fall 16	Fine Dust	1.12	1.32	7.71	—	—	2.45	0.88	0.43	—	2.13	80.23	103.51	89.26	117.25	237.98	236.90	710.89	59.75	12.01	1.35	0.23
Dust-8 Fall 16	Fine Dust	0.97	1.02	7.11	—	—	2.35	0.98	0.41	—	2.10	75.87	113.85	63.72	115.79	219.80	233.22	828.71	83.28	11.34	1.07	0.20
Dust-1 Sum 17	Fine Dust	0.77	0.95	7.18	—	—	2.45	0.69	0.40	—	1.94	73.31	111.54	87.73	119.42	192.56	265.69	623.01	52.31	12.08	0.68	0.40
Dust-5 Sum 17	Fine Dust	0.88	1.10	6.85	—	—	2.39	0.72	0.38	—	1.89	73.37	100.39	71.00	109.78	199.69	240.16	612.80	50.98	11.23	0.88	0.20
Dust-7 Sum 17	Fine Dust	1.37	1.31	8.66	—	—	2.91	1.30	0.45	—	2.37	87.58	113.11	92.41	119.15	222.45	257.46	698.02	57.97	11.56	1.58	0.37
Dust-8 Sum 17	Fine Dust	1.37	1.09	7.56	—	—	2.67	1.43	0.39	—	1.97	76.12	111.80	42.48	109.31	222.43	258.00	727.62	59.56	9.74	1.51	0.05
D5-1 T	A Horizon	0.40	0.46	3.56	40.40	0.12	1.08	0.20	0.24	0.03	1.98	127.38	31.41	47.31	53.56	125.06	301.67	167.06	5.94	6.42	-0.50	-0.03
D5-7 T	A Horizon	0.81	0.69	5.29	36.42	0.21	1.94	1.14	0.34	0.08	2.43	98.63	36.52	74.79	123.67	210.62	322.74	686.04	26.59	12.77	0.61	0.31
D7-AT	A Horizon	0.60	0.71	6.10	36.07	0.10	1.49	0.56	0.39	0.09	2.83	118.46	17.02	43.93	78.88	159.22	265.03	746.47	23.84	16.54	0.08	0.40
D7-CT	A Horizon	0.23	0.20	2.23	42.53	0.12	0.86	0.36	0.12	0.02	1.09	98.63	7.75	66.84	52.52	99.96	207.77	274.41	4.60	6.42	-0.55	-0.69
D7-DT	A Horizon	0.68	0.66	5.04	38.06	0.23	1.47	0.42	0.30	0.10	2.40	118.83	53.43	45.74	85.04	138.99	270.02	289.90	20.23	13.34	0.01	0.19
D8-CT	A Horizon	0.59	0.79	4.66	36.75	0.22	1.77	2.61	0.28	0.10	2.02	98.62	31.37	86.05	96.27	275.89	302.63	827.78	14.36	10.23	1.30	-0.41
D8-DT	A Horizon	0.48	0.68	4.22	37.74	0.25	1.71	1.83	0.26	0.08	1.85	98.63	19.97	84.45	87.36	226.74	299.84	567.37	8.75	11.17	0.72	-0.29
D8-ET	A Horizon	0.79	0.82	5.23	36.43	0.10	1.99	1.74	0.31	0.10	2.35	98.64	22.70	80.40	99.63	239.74	301.89	754.73	12.00	13.26	0.99	-0.03
B1-T	A Horizon	0.37	0.35	2.76	41.93	0.07	1.14	0.44	0.19	0.03	1.34	98.63	25.26	62.59	58.47	113.83	351.74	255.87	8.80	9.11	-0.54	-0.18
B8-T	A Horizon	0.53	0.89	10.94	79.41	0.22	2.80	0.54	0.61	0.05	3.31	131.32	32.98	36.23	107.69	147.49	482.37	351.86	20.60	19.11	-0.15	1.90
D5-1B	B Horizon	0.08	0.22	1.16	44.50	0.08	0.43	0.16	0.08	0.02	0.84	98.64	-0.83	56.98	27.40	90.01	220.45	103.66	4.24	8.02	-0.81	-0.89
D5-7B	B Horizon	0.43	0.51	3.55	39.48	0.15	1.37	1.18	0.25	0.05	1.80	98.63	32.74	62.62	82.94	188.40	322.72	513.69	18.87	14.37	0.17	-0.16
D7-AB	B Horizon	0.41	0.44	3.57	39.83	0.10	1.23	0.42	0.20	0.05	1.80	100.59	30.97	69.80	68.50	120.88	230.70	300.06	12.11	11.16	-0.27	-0.26
D7-CB	B Horizon	0.22	0.12	1.37	44.33	0.08	0.56	0.09	0.06	0.01	0.73	98.64	15.51	75.13	37.63	69.64	171.19	81.76	8.19	6.42	-0.75	-0.99
D7-DB	B Horizon	0.28	0.19	1.80	43.83	0.06	0.60	0.10	0.09	0.02	0.92	98.64	-13.29	58.42	40.71	71.04	188.93	213.44	9.84	10.75	-0.70	-0.84
D8-EB	B Horizon	0.28	0.26	1.92	43.07	0.13	0.77	0.31	0.10	0.02	1.02	98.63	6.81	63.89	49.93	92.13	216.03	199.85	8.09	18.60	-0.55	-0.75
D8-HB	B Horizon	0.55	0.37	3.11	41.08	0.08	1.26	0.32	0.24	0.03	1.33	98.64	27.03	54.75	59.91	127.30	333.69	354.90	22.79	13.51	-0.37	-0.16
B1-B	B Horizon	0.29	0.24	2.38	42.28	0.07	1.04	0.10	0.20	0.02	1.21	98.63	26.08	44.87	51.98	90.20	410.30	188.27	15.06	6.42	-0.96	0.01
B2-B	B Horizon	0.49	0.39	3.51	40.65	0.09	1.43	0.24	0.29	0.02	1.58	102.98	23.46	51.49	59.79	116.57	418.37	273.47	15.01	6.93	-0.62	0.27
D1-R	Rock	0.27	0.14	2.06	43.83	0.04	0.95	0.00	0.05	0.01	0.88	98.63	—	49.27	39.93	73.15	191.43	46.82	12.53	12.31	-0.75	-0.80
D5-R	Rock	0.00	0.10	0.51	46.09	0.05	0.25	0.00	0.02	0.01	0.63	98.63	—	54.47	16.24	76.52	186.81	33.52	5.48	10.52	-0.99	-1.13
D7-R	Rock	0.00	0.09	0.77	45.72	0.05	0.25	0.00	0.01	0.01	0.51	98.62	1.52	52.91	17.79	50.33	181.21	203.98	7.47	6.42	-1.14	-1.09
D-8 ROCKS	Rock	0.01	0.18	0.60	45.91	0.04	0.25	0.00	0.02	0.01	0.59	98.63	18.00	55.81	17.86	57.99	178.88	83.38	7.27	6.42	-0.98	-1.13
DUST1 rock	Rock	0.03	0.06	0.68	—	0.00	0.42	0.04	0.03	0.00	0.96	14.00	—	10.30	12.50	32.30	21.50	37.00	6.50	2.50	-0.89	-1.34
Quartzite-1	Rock	0.00	0.03	0.93	44.74	0.01	0.44	0.04	0.11	0.00	0.69	—	—	—	14.00	31.00	202.00	20.00	—	—	-1.19	-0.86
Quartzite-2	Rock	0.00	0.00	0.37	45.86	0.00	0.15	0.04	0.05	0.00	0.39	—	—	—	7.00	14.00	105.00	—	—	—	-1.10	-1.33
Shale-1	Rock	0.44	0.75	8.84	29.73	0.03	3.21	0.14	0.46	0.05	3.62	—	—	—	120.00	82.00	334.00	598.00	—	—	-0.46	1.68
Shale-2	Rock	0.11	0.72	10.32	28.28	0.05	3.55	0.18	0.57	0.03	3.24	—	—	—	146.00	92.00	260.00	557.00	—	—	-0.38	1.81
Chepeta-1	Rock	0.00	0.11	0.58	45.82	0.06	0.32	0.05	0.06	0.01	0.60	11.00	13.00	—	7.20	28.00	114.00	33.00	7.00	1.40	-1.02	-1.22
Chepeta-2	Rock	0.00	0.17	0.74	45.65	0.07	0.33	0.03	0.06	0.02	0.71	11.00	17.00	—	8.70	25.00	150.00	33.00	7.00	1.90	-1.07	-1.08
Chepeta-3	Rock	0.00	0.11	0.90	45.34	0.07	0.38	0.03	0.06	0.01	0.75	11.00	14.00	—	9.50	24.00	119.00	29.00	5.00	1.80	-1.05	-1.12
Shale-1	Rock	0.00	0.46	6.43	35.82	0.08	3.18	0.07	0.59	0.01	3.45	116.00	71.00	—	125.00	84.00	728.00	420.00	17.00	15.10	-1.58	2.76

Table 3 (continued)

Sample Name	Material	Na %	Mg %	Al %	Si %	P %	K %	Ca %	Ti %	Mn %	Fe %	V ppm	Cr ppm	Cu ppm	Rb ppm	Sr ppm	Zr ppm	Ba ppm	Pb ppm	Th ppm	PC-1	PC-2
Shale-2	Rock	0.00	0.47	6.44	35.67	0.07	3.11	0.07	0.50	0.01	3.83	119.00	56.00	–	114.00	73.00	633.00	399.00	15.00	13.40	−1.52	2.49
Shale-3	Rock	0.00	0.38	5.00	36.04	0.07	2.68	0.06	0.39	0.01	5.91	164.00	53.00	–	94.10	67.00	617.00	361.00	18.00	11.90	−1.87	2.70
Dust mean		0.97	1.08	7.13	–	0.86	2.46	1.11	0.39	–	2.11	76.86	95.95	158.76	111.32	202.07	213.54	683.39	68.50	11.51	1.11	0.13
A mean		0.55	0.63	5.00	42.57	0.17	1.63	0.98	0.30	0.07	2.16	108.78	27.84	62.83	84.31	173.75	310.57	492.15	14.57	11.84	0.20	0.12
B mean		0.34	0.31	2.48	42.12	0.09	0.97	0.33	0.17	0.03	1.25	99.33	16.50	59.77	53.20	107.35	279.15	247.68	12.69	10.69	−0.54	−0.42
Soil mean		0.45	0.47	3.81	42.36	0.13	1.31	0.67	0.24	0.05	1.73	104.30	22.47	61.38	69.57	142.30	295.69	376.35	13.68	11.29	−0.17	−0.14
Rock mean		0.05	0.25	3.01	41.04	0.05	1.30	0.05	0.20	0.01	1.78	76.41	30.44	44.55	49.99	54.02	268.12	203.91	9.84	7.61	−1.07	0.02

pattern of highest values in dust, lowest values in rock, and intermediate values in the soil, consistent with a two-member mixing model (Fig. 5). Mn was not measured in the dust, however the ratio Mn/Fe also decreases from A horizon, to B horizon, to rock. The ratio P/Fe is much higher in dust, and lower in soil and rock samples. The abundance of Si was not quantified in dust, however the ratio Si/Fe is much higher in rock than soil (Fig. 5). Trace elements exhibit a similar pattern, with abundances of Cr, Cu, Rb, Sr, Ba, Pb, and Th attaining their highest values in dust samples and lowest values in rock (Fig. 6, Table 3). Patterns are less clear for V and Zr, both of which attain notably high values in rock samples.

Principle component analysis reveals that 87% of the variance in Na, Mg, Al, K, Ca, Ti, Fe, Rb, Sr, and Zr can be explained by just two components. The first component (PC-1) is dominated by Na, Sr, Mg, and Ca. PC-2 is controlled by Fe, Ti, K, Zr, Rb, and Al. Predictably, values of PC-1 follow the same pattern seen in the major and trace element data, with highest values in dust samples, lowest values in rock, and intermediate values in the soils (Fig. 7, Table 3).

Similar to the major and trace elements, values of $^{87}Sr/^{86}Sr$ and ε_{Nd} exhibit a clear mixing trend with soil samples located midway between end members defined by dust and rock samples (Fig. 8, Table 4). Dust-8 is the only site for which samples of all four materials (dust, A horizon, B horizon, and rock) were analyzed. The five dust samples collected between 2015 and 2019 cluster with $^{87}Sr/^{86}Sr$ values ~ 0.715 and ε_{Nd} between −9 and −11.5. In contrast, the rock sample from this site has a higher $^{87}Sr/^{86}Sr$ of 0.73396, and a much lower ε_{Nd} of −17.1. The soil samples fall between these extremes, with the A horizon more similar to dust, and the B horizon more similar to the rock sample. This same pattern is seen in the overall dataset of 13 dust samples, a pair of A and B horizon samples from Dust-5 the pair from Dust-8, and 8 different rock samples (Fig. 8, Table 4). Although the rock results are more scattered, reflecting variability in different strata of the Uinta Mountain Group, all rock samples exhibit considerably more radiogenic $^{87}Sr/^{86}Sr$ and much more negative ε_{Nd} than their respective soil/dust match. Significantly, soil samples are clearly displayed as a blend between the dust and rock end members (Fig. 8).

The two end-member mixing model used to estimate the fraction of dust (f_{dust}) in soil samples is presented in Fig. 9. The end members are concentration-weighted averages of $^{87}Sr/^{86}Sr$ and ε_{Nd} in rock and dust samples. Values of $^{87}Sr/^{86}Sr$ in the four analyzed soil samples (Table 4) range from 0.71630 to 0.72539. These values intersect the $^{87}Sr/^{86}Sr$ mixing line at an f_{dust} between 0.48 and 0.88. Values of ε_{Nd} in soil samples range from −12.23 to −14.33 (Table 4). These intersect the ε_{Nd} mixing line between 0.43 and 0.80. The zone of mutual overlap for both isotope systems spans from 0.48 to 0.80, corresponding to an estimated dust content in the soil of ~ 50 to 80%.

4. Discussion

4.1. Soil profiles

Previous work has classified soils at the eastern end of the Uinta alpine zone as Inceptic Haplocryalfs, Typic Haplocryolls, and either Typic or Humic Dystrochrepts in the US Soil Taxonomy (Soil Survey Staff, 2014), depending on the thickness of their A horizons and the presence or absence of an argillic horizon (Munroe, 2007). The three deep profiles examined in this study (Dust-1, Dust-7, Dust-8) are consistent with these and other previously published descriptions (Bockheim et al., 2000; Bockheim and Koerner, 1997). Similarly, the contrasting properties of soil A and B horizons noted in this study corroborate previous work in the Uintas, all of which has reported a consistent layer of silt-dominated material capping soil profiles through the alpine zone. This body of previous work has established the ubiquity of this silt cap, classified this material as an alpine loess, noted physical and chemical similarities between this material and modern dust, and explored the possibility that dust deposition is the primary
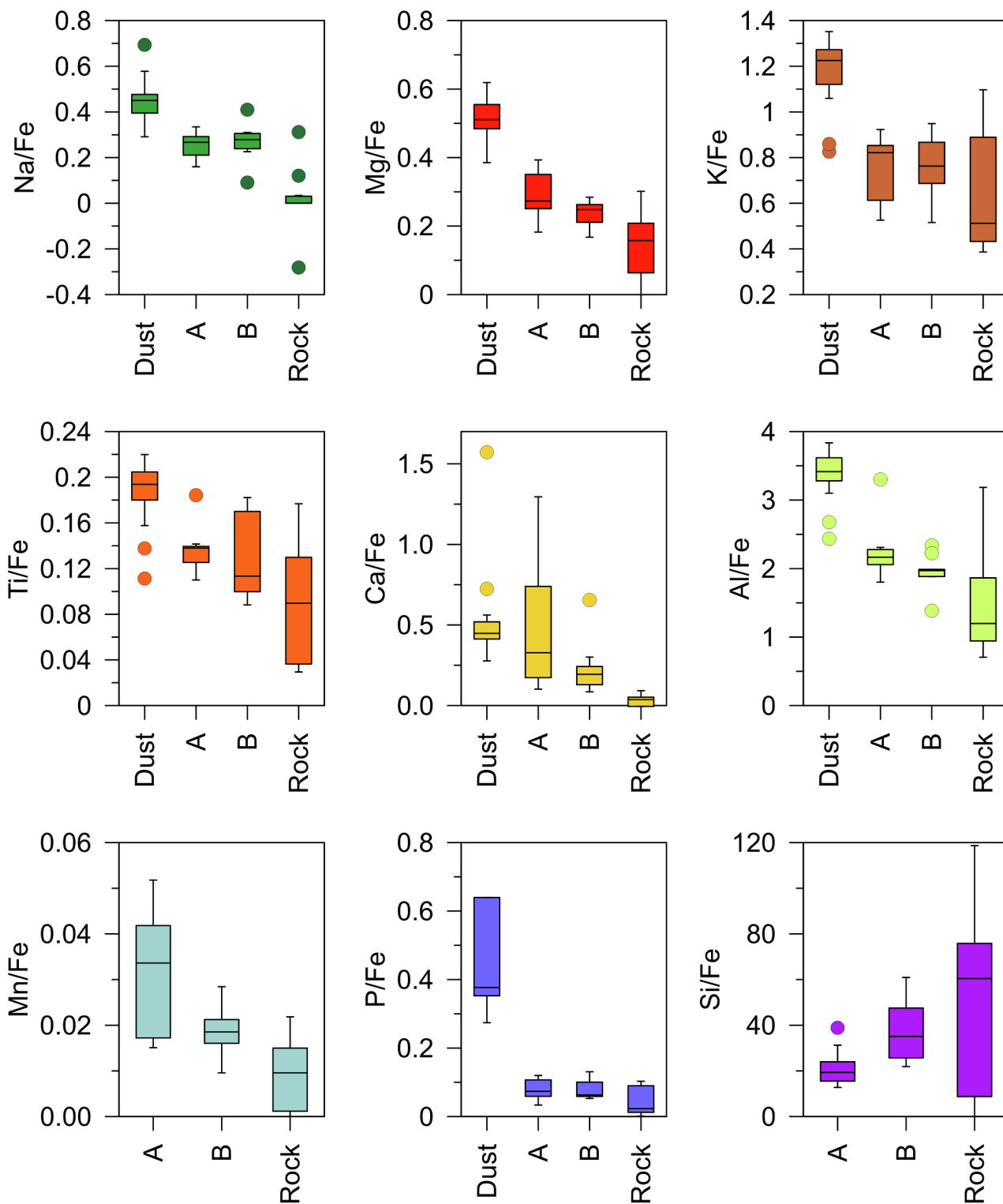
Fig. 5. Boxplots of major element abundances normalized to Fe in dust, A horizon, B horizon, and rock samples. Central lines represent median values, box represents interquartile range, whiskers represent interquartile range × 1.5, and circles represent outliers. In all cases other than Si/Fe, values are greater in dust, lower in rock, and intermediate in soil samples.

source of this fine material (Bockheim et al., 2000; Bockheim and Koerner, 1997; Munroe, 2007; Munroe et al., 2015).

Collectively, soils of the Uinta alpine zone are distinguished by their development from a pair of contrasting parent materials under the influence of pervasive cryoturbation. The autochthonous parent material is congelifractate derived from the underlying bedrock by freeze–thaw-dominated physical weathering (Bryan, 1946). This material inherits its

typical 5YR hues from the reddish-purple colors of the local Uinta Mountain Group bedrock, and its sand-dominated texture reflects the *in situ* disintegration of the sandstone and arkosic members of this bedrock sequence. The presence of subangular to angular coarse fragments, from fine gravel through stone-size, which generally become more abundant with depth, also testifies to the formation of this material through physical weathering of the local bedrock. In contrast, the
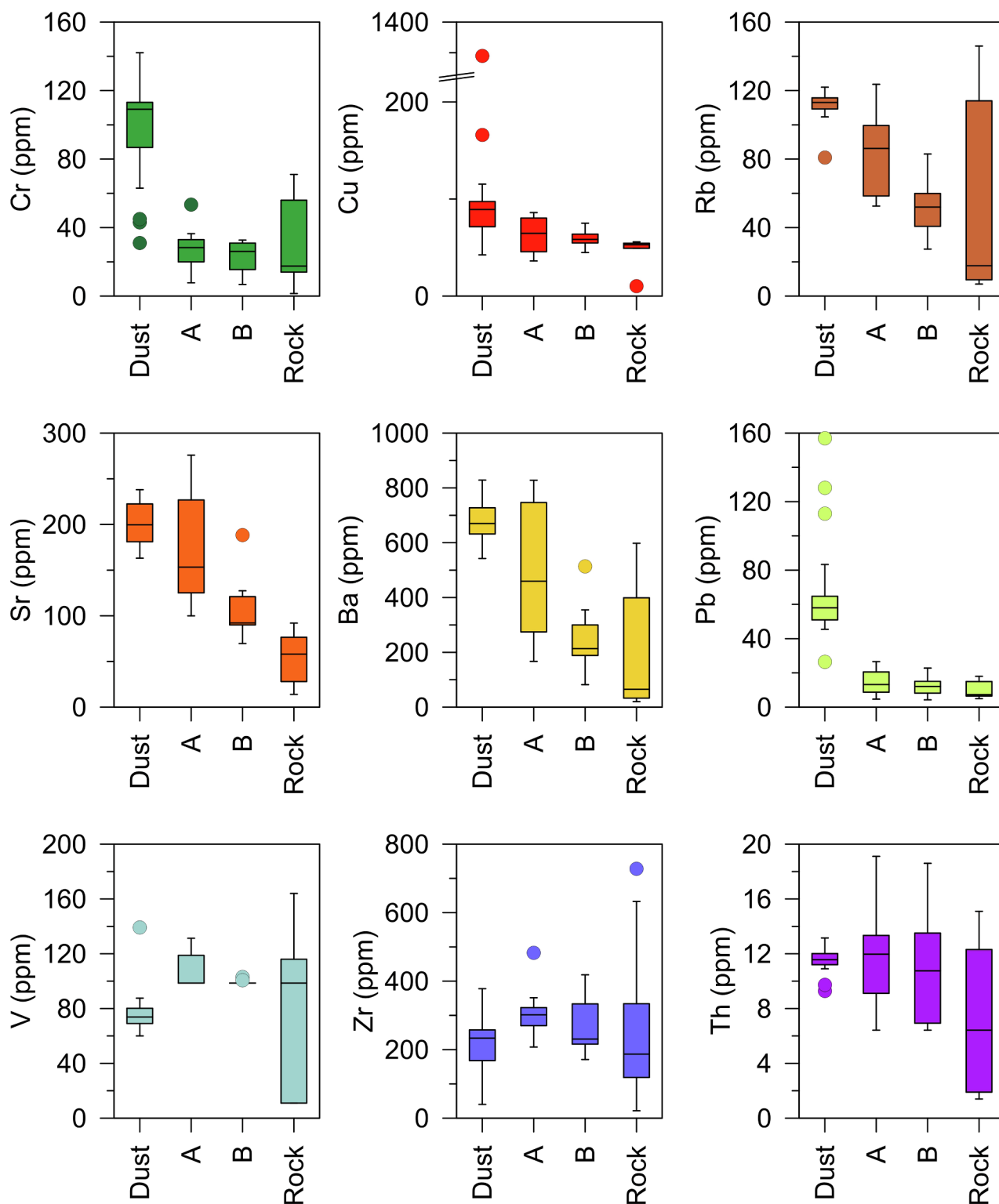
Fig. 6. Boxplots of trace element abundances in dust, A horizon, B horizon, and rock samples. Central lines represent median values, box represents interquartile range, whiskers represent interquartile range × 1.5, and circles represent outliers. In most cases, trace elements are more abundant in dust samples, less abundant in rock, and intermediate in soil A and B horizons. Note the broken Y-axis in the plot for Cu.

allochthonous parent material for these soils is eolian dust. Deposition of this dust forms the capping layer of alpine loess, a well-sorted silt with a grain size distribution, and major and trace element abundances, that strongly contrast with the congelifractate (Figs. 3–7). This loess is added to the soil surface, whereas the congelifractate is introduced into the soil profile from below. Thus, these pedons are located both

spatially and compositionally between two contrasting parent materials. In the formal nomenclature, the A horizons are forming primarily in the alpine loess, whereas the B horizons, which are preceded by "2″, are forming in the congelifractate (Table 2).

Cryoturbation is evidenced in these soils (Fig. 2) by wavy and irregular horizon boundaries, isolated pockets of one horizon material
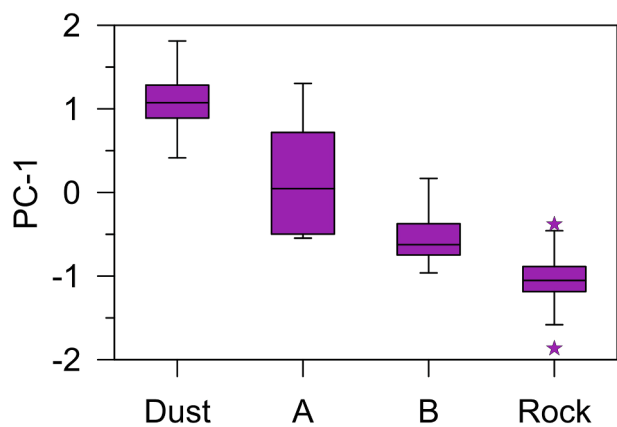
Fig. 7. Boxplot of the first principle component (PC-1) in dust, A horizon, B horizon, and rock samples. Central lines represent median values, box represents interquartile range, whiskers represent interquartile range × 1.5, and stars represent outliers. PC-1 was determined for the 10 elements measured in all sample types (Na, Mg, Al, K, Ca, Ti, Fe, Rb, Sr, and Zr) using a varimax rotation and an eigenvalue extraction threshold of 1. Values are clearly highest in dust samples, lowest in rock, and intermediate in soil horizons.

within another, and by oriented clasts (Ahrens et al., 2004; Bockheim et al., 1997). The presence of strongly developed platy structure in some horizons is a further indication that the growth and decay of ice lenses is a significant process in these soil profiles (Table 2). Notably, despite the subzero mean annual temperature and presence of cryoturbated ("gelic") material within 100 cm of the soil surface (Bockheim et al., 1997), these profiles are not classified as Gelisols (Soil Survey Staff, 2014) because it is unknown whether permafrost is present within 200 cm of the ground surface. When these pits were excavated in late summer, soil temperatures at 50 cm were 3–5 °C. On the other hand, data loggers buried for four years (2005–2009) at a depth of 50 cm in similar soil profiles at a site 1.5 km west of, and 300 m lower than, Dust-8 revealed mean soil temperatures ~ 0 °C. Likewise, average 50-cm soil temperatures at a site 3 km west of Dust-1 (at the same elevation) were −1.5 to −2.5 °C during the same time period (Bockheim and Munroe, 2014 and Munroe, unpublished). Thus, permafrost may be

present within the upper 2-m of some Uinta alpine soil pedons, meaning that these soils would be classified as Gelisols in the suborder Turbels (Soil Survey Staff, 2014).

4.2. Pedogenesis

A model for the long-term formation of these soils was presented by Munroe (2007). A key consideration in this model is the reality that, given their location above the glacial limit, these soils have experienced potentially numerous glacial-interglacial cycles. The well-developed patterned ground (Fig. 1) that characterizes the alpine zone of the Uintas indicates that large-scale cryoturbation occurs at times in this environment. On the other hand, much of this patterned ground appears stabilized under modern climate conditions, on the basis of lichen cover on rocks and continuous vegetation in polygon centers. Thus, while cryoturbation is probably occurring to a modest degree under the modern periglacial climate, more intense mixing likely occurs under the colder climates characterizing glaciations, or during the transitions between interglacial and glacial conditions (Munroe, 2007).

A second consideration in this pedogenic model is the observation that the thickness of the loess layer is essentially consistent over a variety of landscape positions, including the periglacial upland and forested glacial moraines at lower elevations (Bockheim et al., 2000; Munroe, 2007). This consistency suggests that the modern layer of loess accumulated across the entire landscape after the last glaciation. This interpretation is not meant to imply that dust deposition only occurs under interglacial conditions; abundant evidence indicates that global dust transport was greater during the Last Glacial Maximum (e.g. Harrison et al., 2001; Maher et al., 2010), and this situation likely affected the Uintas as well. Rather, it appears that dust deposited in the Uinta alpine zone during glacial times was directly mixed into the solum by cryoturbation. Alternatively, the likely absence of widespread plant cover on the landscape during glaciations may have greatly reduced loess trapping rates (Yang et al., 2020, Yang et al., 2016). Only during interglacial conditions, when cryoturbation is reduced and the landscape is extensively vegetated, can a discrete layer of dust accumulate as a cap of alpine loess at the top of the soil profile.

Looking forward, with this model as a starting point, the currently ubiquitous layer of loess capping these soil profiles is destined to be
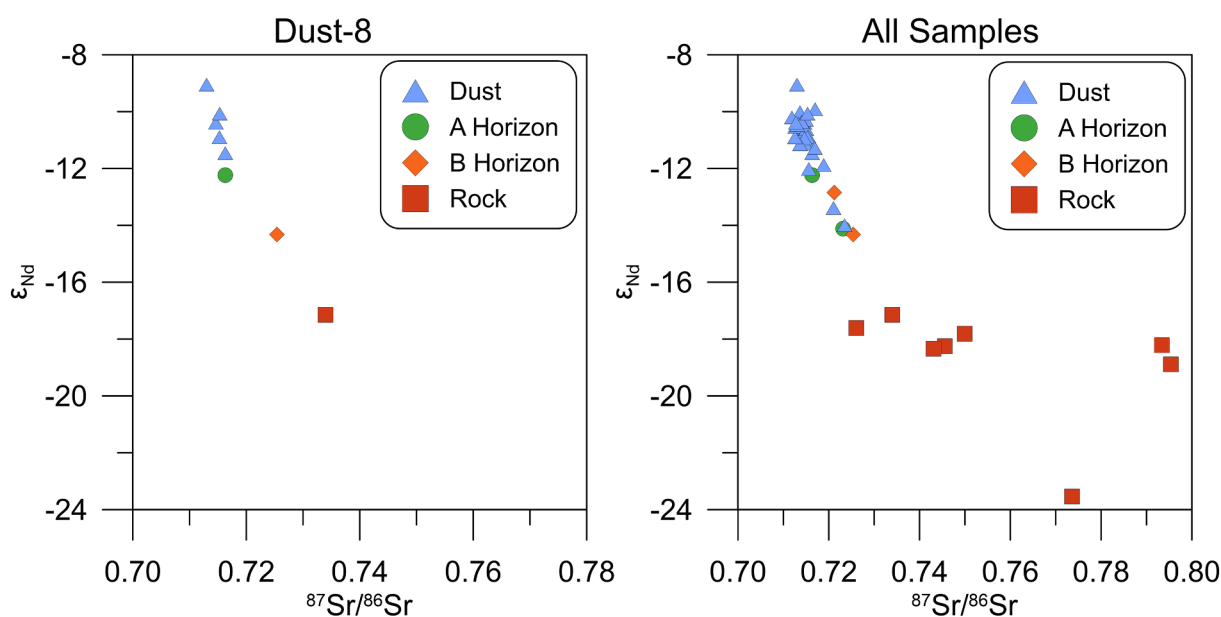

Fig. 8. Scatterplots of $^{87}Sr/^{86}Sr$ and ε_{Nd} in samples of dust, soil, and rock. Left figure presents values for Dust-8, the only site for which all four types of material were analyzed. The figure on the right presents the entire set of results from all sites. In both figures it is clear that soil samples exist along a mixing line between a dust and rock end members. A horizons also more closely resemble dust than B horizons do.

Table 4
Isotope Measurements of Dust, Soil, and Rock Samples.

Lab Number	Sample ID	Material	Dust-x*	Collection	Analyzed	Rb ppm	Sr ppm	$^{87}Sr/^{86}Sr$	2-σ	Sm ppm	Nd ppm	$^{143}Nd/^{144}Nd$	2-σ	ε^{143}Nd	2-σ	**
7Sr-15	JSM-17-2	Dust	2	Aug 2016	2017	114	196	0.71497	0.000011	6	14	0.51207	0.000007	−10.96	0.14	1
7Sr-16	JSM-17-3	Dust	3	Aug 2016	2017	115	290	0.71331	0.000011	6	14	0.51209	0.000007	−10.53	0.14	1
7Sr-18	JSM-17-5	Dust	5	Aug 2016	2017	113	198	0.71602	0.000010	7	16	0.51207	0.000007	−11.04	0.14	1
7Sr-19	JSM-17-6	Dust	7	Aug 2016	2017	105	214	0.71480	0.000011	8	19	0.51206	0.000007	−11.13	0.14	1
7Sr-20	JSM-17-7	Dust	8	Aug 2016	2017	81	233	0.71300	0.000009	6	13	0.51217	0.000007	−9.05	0.14	1
7Sr-22	JSM-17-9	Dust	S	Aug 2016	2017	–	–	0.71699	0.000011	–	–	0.51213	0.000008	−9.92	0.16	1
7Sr-23	JSM-17-10	Dust	1	Oct 2016	2017	112	215	0.71511	0.000011	6	15	0.51208	0.000008	−10.86	0.16	1
7Sr-24	JSM-17-11	Dust	2	Oct 2016	2017	117	217	0.71364	0.000013	7	15	0.51212	0.000007	−10.02	0.14	1
7Sr-25	JSM-17-12	Dust	3	Oct 2016	2017	116	238	0.71330	0.000011	6	14	0.51210	0.000007	−10.44	0.14	1
7Sr-26	JSM-17-13	Dust	5	Oct 2016	2017	115	226	0.71399	0.000011	6	15	0.51209	0.000006	−10.61	0.12	1
7Sr-27	JSM-17-14	Dust	6	Oct 2016	2017	121	251	0.71398	0.000011	6	14	0.51209	0.000007	−10.58	0.14	1
7Sr-28	JSM-17-15	Dust	7	Oct 2016	2017	117	238	0.71459	0.000009	6	14	0.51208	0.000007	−10.71	0.14	1
7Sr-29	JSM-17-16	Dust	8	Oct 2016	2017	116	220	0.71466	0.000010	6	13	0.51210	0.000008	−10.39	0.16	1
8SR-22	MIDD-18-2	Dust	2	Jun 2017	2018	115	231	0.71329	0.000009	6	14	0.51210	0.000007	−10.41	0.13	1
8SR-23	MIDD-18-3	Dust	3	Jun 2017	2018	117	237	0.71261	0.000011	6	13	0.51209	0.000008	−10.53	0.16	1
8SR-25	MIDD-18-5	Dust	5	Jun 2017	2018	110	200	0.71505	0.000010	6	13	0.51209	0.000013	−10.62	0.26	1
8SR-26	MIDD-18-6	Dust	6	Jun 2017	2018	125	250	0.71185	0.000010	7	15	0.51211	0.000007	−10.20	0.14	1
8SR-27	MIDD-18-7	Dust	7	Jun 2017	2018	119	222	0.71554	0.000010	6	14	0.51208	0.000002	−10.88	0.04	1
8SR-28	MIDD-18-8	Dust	8	Jun 2017	2018	109	222	0.71526	0.000011	5	12	0.51208	0.000009	−10.90	0.17	1
8SR-30	MIDD-18-10	Dust	S	Jun 2017	2018	–	–	0.71499	0.000010	–	–	0.51211	0.000014	−10.30	0.27	1
20SR-11	PO-1C	Dust	1	Oct 2019	2020	93	188	0.71885	0.000009	5	27	0.51203	0.000010	−11.88	0.19	2
20SR-13	PO-2C	Dust	2	Oct 2019	2020	89	192	0.71466	0.000011	5	28	0.51207	0.000009	−10.93	0.18	2
20SR-15	PO-3C	Dust	3	Oct 2019	2020	92	205	0.71366	0.000010	5	27	0.51206	0.000008	−11.15	0.16	2
20SR-17	PO-4C	Dust	4	Oct 2019	2020	105	179	0.72349	0.000012	6	30	0.51192	0.000010	−13.99	0.19	2
20SR-19	PO-5C	Dust	5	Oct 2019	2020	91	193	0.71561	0.000010	5	29	0.51202	0.000010	−12.02	0.19	2
20SR-21	PO-6C	Dust	6	Oct 2019	2020	90	214	0.71256	0.000010	5	28	0.51207	0.000009	−10.91	0.17	2
20SR-23	PO-8C	Dust	8	Oct 2019	2020	92	175	0.71256	0.000010	5	25	0.51205	0.000009	−11.46	0.17	2
20SR-12	PO-1F	Dust	1	Oct 2019	2020	126	192	0.71693	0.000010	8	41	0.51206	0.000009	−11.29	0.17	2
20SR-14	PO-2F	Dust	2	Oct 2019	2020	123	187	0.71402	0.000011	7	37	0.51210	0.000009	−10.36	0.18	2
20SR-16	PO-3F	Dust	3	Oct 2019	2020	130	189	0.71306	0.000010	7	40	0.51210	0.000009	−10.48	0.18	2
20SR-18	PO-4F	Dust	4	Oct 2019	2020	129	182	0.72105	0.000010	7	40	0.51195	0.000011	−13.39	0.22	2
20SR-20	PO-5F	Dust	5	Oct 2019	2020	124	205	0.71404	0.000010	7	40	0.51210	0.000011	−10.37	0.22	2
20SR-22	PO-6F	Dust	6	Oct 2019	2020	130	194	0.71276	0.000011	7	39	0.51210	0.000010	−10.40	0.20	2
20SR-24	PO-8F	Dust	8	Oct 2019	2020	124	181	0.71534	0.000011	6	34	0.51212	0.000008	−10.07	0.15	2
8SR-37	MIDD-18-17	A Horizon	5	Jun 2017	2018	55	121	0.72318	0.000010	–	–	0.51191	0.000006	−14.12	0.12	2
8SR-35	MIDD-18-15	A Horizon	8	Jun 2017	2018	98	238	0.71630	0.000010	–	–	0.51201	0.000014	−12.23	0.28	2
8SR-38	MIDD-18-18	B Horizon	5	Jun 2017	2018	38	83	0.72123	0.000010	–	–	0.51198	0.000010	−12.84	0.19	2
8SR-36	MIDD-18-16	B Horizon	8	Jun 2017	2018	46	96	0.72539	0.000010	–	–	0.51190	0.000005	−14.33	0.10	2
Rock-1	MIDD-18-11	Rock	1	–	2018	13	32	0.74556	0.000009	–	–	0.51170	0.000000	−18.26	0.00	1
Rock-2	MIDD-18-12	Rock	2	–	2018	24	66	0.72604	0.000010	–	–	0.51173	0.000027	−17.61	0.54	1
Rock-4	MIDD-18-13	Rock	4	–	2018	22	41	0.77363	0.000011	–	–	0.51143	0.000021	−23.54	0.40	1
Rock-8	MIDD-18-14	Rock	8	–	2018	–	–	0.73396	0.000012	–	–	0.51176	0.000002	−17.14	0.04	1
Chepeta-1	20SR-25	Rock	1	–	2020	7	28	0.74309	0.000013	1	5	0.51169	0.000011	−18.34	0.22	2
Chepeta-2	20SR-26	Rock	2	–	2020	9	25	0.74992	0.000018	1	5	0.51172	0.000014	−17.82	0.28	2
Bollie-1	20SR-27	Rock	1	–	2020	125	84	0.79337	0.000011	6	36	0.51170	0.000011	−18.21	0.22	2
Bollie-2	20SR-28	Rock	2	–	2020	114	73	0.79540	0.000011	5	29	0.51167	0.000011	−18.89	0.22	2

*Dust collector number.
**Reference: 1 – Munroe et al., 2019; 2-this study.
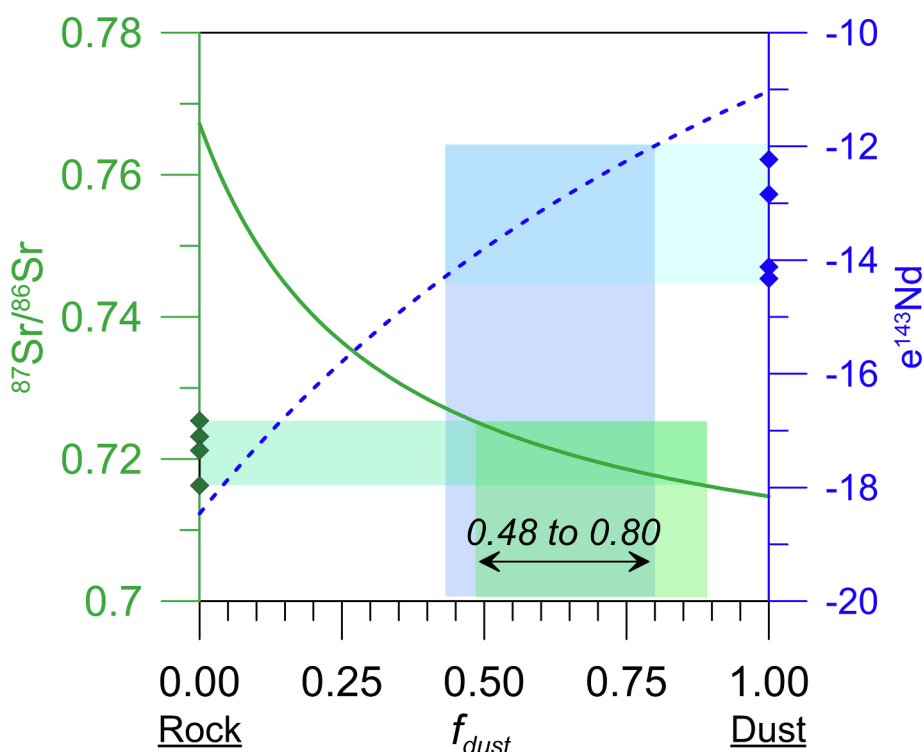
Fig. 9. Calculation of the dust fraction (f_{dust}) in soil samples from end-member mixing models based on ^{87}Sr/^{86}Sr (green solid line) and ε_{Nd} (blue dashed line). End member values for rock (left side) and dust (right side) are concentration-weighted averages. Diamonds represent the values of ^{87}Sr/^{86}Sr and ε_{Nd} determined for four soil samples (Table 4). The 2σ error ranges around these values intersect their respective mixing lines in fields that overlap between f_{dust} of 0.48 and 0.80, corresponding to a range of dust content in the soil from ~ 50 to 80%.

incorporated into the deeper solum when cryoturbation again increases in response to colder conditions at the transition to the next orbitally-driven glaciation. Over the time-scale of glacial-interglacial cycles, therefore, loess that is archived at the soil surface during interglaciations is mixed downward into the congelifractate during glaciations (or climatic transitions), resulting in a general trend of increasing coarseness with depth, and strongly contrasting ratios of Clay/Sand and (Clay + Silt)/Sand in A and B horizons. Similarly, frost heave lifts gravel, cobbles, and stones upward through the solum so that some coarse material is present in the A horizon formed within the loess cap.

4.3. Dust content of alpine soils and implications

A key objective of this study was quantifying the degree to which long-term dust deposition impacts soil development in the Uinta alpine zone. From the horizonation exhibited in these soils, and the contrasting physical and chemical properties of surface and subsurface horizons, it is clear that dust deposition is a key component of pedogenesis in this study area. The mixing model approach applied to dust and congelifractate end members, defined in terms of ^{87}Sr/^{86}Sr and ε_{Nd}, reveals that at least half of the material in a soil profile is exogenous dust. Thus, dust deposition, coupled with intense cryoturbation, has greatly affected the physical and chemical properties of these soils.

Previous work has employed a similar approach to estimate the portion of soil profiles resulting from accretion of eolian dust in the San Juan Mountains (Fig. 1) of southwestern Colorado (Lawrence et al., 2011). In that work, which used both ^{87}Sr/^{86}Sr and ε_{Nd}, it was estimated that 10–40% of the mass of soil profiles was delivered through dust deposition. This estimate is lower than for the Uintas, however the Colorado study area was glaciated during the Last Glacial Maximum (Lawrence et al., 2011). Thus, the soils studied there, and the dust contained within them, are likely post-glacial features. The greater dust content of Uinta alpine soil profiles is consistent with the fact that significant parts of the Uinta landscape are considerably older. Along those lines, it is also notable that the soil profiles in the Colorado study were shallower (40–60 cm) and did not contain B horizons (Lawrence et al., 2011). The greater depth and horizonation of the Uinta alpine

soils, therefore, is also consistent with their greater age. Overall, the results reported from the Uintas demonstrate that older soils above the glacial limit are both better developed and contain more dust than glaciated soils in a mountain setting. This interpretation matches previous studies concluding that eolian sediments can be a primary parent material for alpine soils (e.g. Gild et al., 2018; Küfmann, 2008, 2003; Lin and Feng, 2015; Yang et al., 2016).

Long-term dust deposition, combined with cryoturbation to incorporate this dust into soil profiles, has also affected the chemical properties of Uinta alpine soils. Figs. 5–7, and Table 3, make it clear that dust is geochemically distinct from the Uinta bedrock. One major difference is the greater abundance of P in dust, which previous work has established is generally 30–40 × more abundant in Uinta dust than in local bedrock (Munroe, 2014; Munroe et al., 2015). Given an average P content of 4000 ppm (4 mg/g) in Uinta dust (Munroe et al., 2015), and an average rate of dust deposition of 3.5 g/m^2/yr (Munroe, 2014), 14 mg of P accumulates over each square meter of the alpine zone each year (equivalent to 320 g P$_2$O$_5$ per hectare/yr). Given the low P values in Uinta bedrock (average of 112 ppm, 0.112 mg/g), the long-term impact of this eolian P, coming from a combination of natural and anthropogenic sources (Brahney et al., 2014; Okin et al., 2004; Zhang et al., 2018), is likely significant for primary productivity in this alpine ecosystem.

Previous work has noted the high fertility of Uinta alpine soils, which commonly have base saturation > 50%, and exchangeable bases (Ca + Mg + K + Na) in excess of 400 kmol/ha (Munroe et al., 2015). Furthermore, plant species common in the Uinta alpine zone, such as *Acomastylis rossii*, have been shown to contain high contents of Ca (Bockheim et al., 2000). Similar to P, the abundance of Ca is considerably higher (~20 ×) in dust arriving in the Uintas relative to local bedrock (Munroe, 2014). Thus it seems likely that dust is a source for much of the Ca and other base cations in Uinta alpine soils.

Together these observations regarding P and Ca support the conclusion that the fertility of Uinta alpine soils is primarily a function of long-term dust deposition. A similar finding was reached by work in the Sierra Nevada of California (Fig. 1), which demonstrated that the flux of P delivered through dust deposition was greater than the flux of P

derived from weathering of local bedrock (Aciego et al., 2017). In light of this result, it is notable that the average concentration of P in Uinta dust (4 mg/g) is greater than in the Sierra Nevada (~1.5 mg/g), and that the average abundance of P in Uinta bedrock is at the low end of the range of averages values reported for rocks in the Sierra Nevada (0.12 ± 0.01 to 0.61 ± 0.02 mg/g). The relative importance of P delivered to the Uintas by dust is, therefore, likely even greater than that quantified for the Sierra Nevada.

4.4. Direction for future work

The results of this study support the first estimates for the dust content in alpine soils of the Uinta Mountains, and indicate that high-elevations soils in unglaciated environments can be strongly influenced by long-term dust deposition. Nonetheless, there are several directions for future work that would strengthen the interpretations presented here. One goal would be the collection and analysis of additional rock samples to better constrain the geochemical properties of sections of the Uinta Mountain Group that are weathering beneath the alpine soils. This is difficult because bedrock exposures are rare on the soil-mantled crest of the Uintas, however additional field reconnaissance might identify areas where bedrock can be accessed. A related challenge is that collection of additional rock samples should be aimed at the full suite of rock types represented by the Uinta Mountain Group, yet it is the more resistant quartz-dominated units that are likely to be exposed and available for sampling. The less resistant shale layers are unlikely to form outcrops, however their potentially more variable geochemistry may make them an important, and currently poorly constrained, component of the congelifractate.

The existing network of passive dust collectors has provided useful information about modern dust in the alpine zone of the Uintas. However, these collectors are from individual locations that are considered broadly representative of the surrounding landscape. Focused deployment of multiple collectors in close proximity to one another could reveal differences in dust flux at finer scales related to microtopographic, snowcover, or aspect controls that play a role in soil formation (e.g. Hiller et al., 2005; Holtmeier and Broll, 1992).

Excavation of deeper soil profiles, ideally extending through the solum down to saprolite or relatively unweathered bedrock, would be useful for better quantifying the total amount of exogenous material that has been added to the Uinta alpine zone over time. Unfortunately, given site restrictions that mandate reliance on hand-excavation, it is unclear if it would be physically possible to access material deeper than the ~ 100 cm achieved in previous soil pits.

Finally, additional geochemical approaches might improve estimates of f_{dust} in these soils. For instance, in addition to $^{87}Sr/^{86}Sr$ and ε_{Nd}, analysis of Hf or Pb isotopes might allow further distinctions to be drawn between dust and local rock (e.g. Moreno et al., 2006; Zhao et al., 2014). Similarly, full trace-element characterization of soil and rock samples, matching that previously conducted for dust samples, could refine the principle component analysis presented here. On the other hand, although these approaches might support refinement of the f_{dust} estimates, it is unlikely they would change the overall conclusion that alpine soils in the Uinta Mountains contain an appreciable amount of eolian dust.

5. Conclusion

Field and laboratory study of alpine soils at four locations in the Uinta Mountains of northeastern Utah emphasize the degree to which pedogenesis in this environment has been influenced by long-term additions of eolian sediment. Soil profiles exhibit considerable evidence for cryoturbation, consistent with the periglacial environment (mean annual temperature of −2°C) on this high-elevation (> 3500 m), unglaciated upland. Paired samples demonstrate that soil A horizons are consistently finer-grained than B horizons. All soil samples contain a

prominent mode of 10–15-μm silt, identical to that observed in modern dust samples. Together these observations support previous reports of a ubiquitous layer of alpine loess capping soil profiles in this environment. Abundances of major and trace elements, along with measurements of $^{87}Sr/^{86}Sr$ and ε_{Nd}, clearly indicate that soil samples are a mixture between allochthonous dust and an autochthonous congelifractate derived from the local bedrock. End-member mixing models based on $^{87}Sr/^{86}Sr$ and ε_{Nd} reveal that soil samples contain ~ 50 to 80% dust. Because this periglacial upland was not glaciated during the Pleistocene, these soils have been forming for much longer than the post-glacial soils at lower elevations within glacial valleys. Eolian additions over time, therefore, have collectively enriched these soils in fine-grained, nutrient-rich material with significant concomitant effects on pedogenesis and soil fertility.

Declaration of Competing Interest

The authors declare that they have no known competing financial interests or personal relationships that could have appeared to influence the work reported in this paper.

References

Aciego, S.M., Riebe, C.S., Hart, S.C., Blakowski, M.A., Carey, C.J., Aarons, S.M., Dove, N.C., Botthoff, J.K., Sims, K.W.W., Aronson, E.L., 2017. Dust outpaces bedrock in nutrient supply to montane forest ecosystems. Nat. Commun. 8, 14800.

Ahrens, R.J., Bockheim, J.G., Ping, C.L., 2004. The Gelisol order in soil taxonomy. Cryosols. Springer 627–635.

Arcusa, S.H., McKay, N.P., Routson, C.C., Munoz, S.E., 2019. Dust-drought interactions over the last 15,000 years: A network of lake sediment records from the San Juan Mountains, Colorado. Holocene 0959683619875192.

Birkeland, P.W., Burke, R.M., Shroba, R.R., 1987. Holocene alpine soils in gneissic cirque deposits, Colorado Front Range. U.S. Geol. Survey Bullet. 1590, E1–E21.

Bockheim, J., Koerner, D., 1997. Pedogenesis in alpine ecosystems of the eastern Uinta Mountains, Utah. USA. Arct. Alp. Res. 29, 164–172.

Bockheim, J., Munroe, J., Douglass, D., Koerner, D., 2000. Soil development along an elevational gradient in the southeastern Uinta Mountains, Utah, USA. Catena 39, 169–185.

Bockheim, J.G., Munroe, J.S., 2014. Organic carbon pools and genesis of alpine soils with permafrost: A review. Arct. Antarct. Alp. Res. 46, 987–1006.

Bockheim, J.G., Tarnocai, C., Kimble, J.M., Smith, C.A.S., 1997. The concept of gelic materials in the new Gelisol order for permafrost-affected soils. Soil Sci. 162, 927–939.

Bradley, M.D., 1995. Timing of the Laramide rise of the Uinta Mountains, Utah and Colorado. Guidebook – Wyom. Geol. Assoc. 1995, 31–44.

Brahney, J., Ballantyne, A., Kociolek, P., Spaulding, S., Otu, M., Porwoll, T., Neff, J., 2014. Dust mediated transfer of phosphorus to alpine lake ecosystems of the Wind River Range, Wyoming, USA. Biogeochemistry 1–20.

Bryan, K., 1946. Cryopedology, the study of frozen ground and intensive frost-action, with suggestions on nomenclature. Am. J. Sci. 244, 622–642.

Clark, P.U., Dyke, A.S., Shakun, J.D., Carlson, A.E., Clark, J., Wohlfarth, B., Mitrovica, J.X., Hostetler, S.W., McCabe, A.M., 2009. The last glacial maximum. Science 325, 710–714. https://doi.org/10.1126/science.1172873.

Colville, E.J., Carlson, A.E., Beard, B.L., Hatfield, R.G., Stoner, J.S., Reyes, A.V., Ullman, D.J., 2011. Sr-Nd-Pb isotope evidence for ice-sheet presence on southern greenland during the last interglacial. Science 333, 620–623. https://doi.org/10.1126/science.1204673.

Condie, K.C., Lee, D., Farmer, G.L., 2001. Tectonic setting and provenance of the Neoproterozoic Uinta Mountain and Big Cottonwood groups, northern Utah: Constraints from geochemistry, Nd isotopes, and detrital modes. Sed. Geol. 141, 443–464.

Dahms, D.E., 1993. Mineralogical evidence for eolian contribution to soils of late Quaternary moraines, Wind River Mountains, Wyoming, USA. Geoderma 59, 175–196.

Dahms, D.E., Rawlins, C.L., 1996. A two-year record of eolian sedimentation in the Wind River Range, Wyoming, U.S.A. Arct. Alp. Res. 28, 210–216.

Dean Jr, W.E., 1974. Determination of carbonate and organic matter in calcareous sediments and sedimentary rocks by loss on ignition; comparison with other methods. J. Sediment. Petrol. 44, 242–248. https://doi.org/10.1306/74D729D2-2B21-11D7-8648000102C1865D.

Dehler, C.M., Porter, S.M., De Grey, L.D., Sprinkel, D.A., Brehm, A., 2007. The Neoproterozoic Uinta Mountain Group revisited; a synthesis of recent work on the Red Pine Shale and related undivided clastic strata, northeastern Utah, U. S. A. Special Publ. – Soc. Sedim. Geol. 86, 151–166.

Dia, A., Chauvel, C., Bulourde, M., Gerard, M., 2006. Eolian contribution to soils on Mount Cameroon; isotopic and trace element records. Chem. Geol. 226, 232–252. https://doi.org/10.1016/j.chemgeo.2005.09.022.

Dymond, J., Biscaye, P.E., Rex, R.W., 1974. Eolian origin of mica in hawaiian soils. Geol. Soc. Am. Bull. 85, 37–40.

Faure, G., 1997. Principles and Applications of Geochemistry. Prentice Hall Upper Saddle River, NJ.

Gild, C., Geitner, C., Sanders, D., 2018. Discovery of a landscape-wide drape of late-glacial aeolian silt in the western Northern Calcareous Alps (Austria): First results and implications. Geomorphology 301, 39–52.

Harrison, S.P., Kohfeld, K.E., Roelandt, C., Claquin, T., 2001. The role of dust in climate changes today, at the last glacial maximum and in the future. Earth-Sci. Rev. Recent Res. Loess Palaeosols, Pure Appl. 54, 43–80. https://doi.org/10.1016/S0012-8252(01)00041-1.

Heindel, R.C., Putman, A.L., Murphy, S.F., Repert, D.A., Hinckley, E.-L.S., 2020. Atmospheric Dust Deposition Varies by Season and Elevation in the Colorado Front Range, USA. Journal of Geophysical Research: Earth Surface 125, e2019JF005436. https://doi.org/10.1029/2019JF005436.

Hiller, B., Nuebel, A., Broll, G., Holtmeier, F.-K., 2005. Snowbeds on Silicate Rocks in the Upper Engadine (Central Alps, Switzerland)—Pedogenesis and Interactions among Soil, Vegetation, and Snow Cover. Arct. Antarct. Alp. Res. 37, 465–476. https://doi.org/10.1657/1523-0430(2005)037[0465:SOSRIT]2.0.CO;2.

Holtmeier, F.-K., Broll, G., 1992. The influence of tree islands and microtopography on pedoecological conditions in the forest-alpine tundra ecotone on Niwot Ridge, Colorado Front Range, USA. Arct. Alp. Res. 24, 216–228.

Huggett, R.J., 1975. Soil landscape systems: a model of soil genesis. Geoderma 13, 1–22.

Johnston, S.W., 2001. The influence of aeolian dust deposits on alpine soils in south-eastern Australia. Soil Res. 39, 81–88. https://doi.org/10.1071/sr99121.

Küfmann, C., 2008. Are cambisols in alpine karst autochthonous or eolian in origin? Arct. Antarct. Alp. Res. 40, 506–518. https://doi.org/10.1657/1523-0430(06-091)[KUEFMANN]2.0.CO;2.

Küfmann, C., 2003. Soil types and eolian dust in high-mountainous karst of the Northern Calcareous Alps (Zugspitzplatt, Wetterstein Mountains, Germany). Catena 53, 211–227.

Kurtz, A.C., Derry, L.A., Chadwick, O.A., 2001. Accretion of Asian dust to Hawaiian soils; isotopic, elemental, and mineral mass balances. Geochim. Cosmochim. Acta 65, 1971–1983. https://doi.org/10.1016/S0016-7037(01)00575-0.

Laabs, B.J.C., Carson, E.C., 2005. Glacial geology of the southern Uinta Mountains, in: Dehler, C.M., Pederson, J.L., Sprinkel, D.A., Kowallis, B.J. (Eds.), Uinta Mountain Geology. Utah Geological Survey, pp. 235–253.

Laabs, B.J.C., Refsnider, K.A., Munroe, J.S., Mickelson, D.M., Applegate, P.J., Singer, B.S., Caffee, M.W., 2009. Latest Pleistocene glacial chronology of the Uinta Mountains: Support for moisture-driven asynchrony of the last deglaciation. Quat. Sci. Rev. 28, 1171–1187. https://doi.org/10.1016/j.quascirev.2008.12.012.

Lawrence, C.R., Neff, J.C., 2009. The contemporary physical and chemical flux of aeolian dust; a synthesis of direct measurements of dust deposition. Chem. Geol. 267, 46–63. https://doi.org/10.1016/j.chemgeo.2009.02.005.

Lawrence, C.R., Neff, J.C., Farmer, G.L., 2011. The accretion of aeolian dust in soils of the San Juan Mountains, Colorado, USA: Dust accretion in the san juan mountains. J. Geophys. Res. 116 (F2). https://doi.org/10.1029/2010JF001899.

Lawrence, C.R., Painter, T.H., Landry, C.C., Neff, J.C., 2010. Contemporary geochemical composition and flux of aeolian dust to the San Juan Mountains, Colorado, United States. J. Geophys. Res. 115, G03007. https://doi.org/10.1029/2009JG001077.

Lawrence, C.R., Reynolds, R.L., Ketterer, M.E., Neff, J.C., 2013. Aeolian controls of soil geochemistry and weathering fluxes in high-elevation ecosystems of the Rocky Mountains. Colorado. Geochim. Cosmochim. Acta 107, 27–46.

Li, J., Zhang, G., Ruan, L., Yang, J., Wang, H., 2016. Sr–Nd elements and isotopes as tracers of dust input in a tropical soil chronosequence. Geoderma 262, 227–234.

Lin, Y.-C., Feng, J.-L., 2015. Aeolian dust contribution to the formation of alpine soils at Amdo (Northern Tibetan Plateau). Geoderma 259–260, 104–115. https://doi.org/10.1016/j.geoderma.2015.05.012.

Litaor, M.I., 1987. The influence of eolian dust on the genesis of alpine soils in the Front Range. Colorado. Soil Sci. Soc. Am. J. 51, 142–147.

Maher, B.A., Prospero, J.M., Mackie, D., Gaiero, D., Hesse, P.P., Balkanski, Y., 2010. Global connections between aeolian dust, climate and ocean biogeochemistry at the present day and at the last glacial maximum. Earth Sci. Rev. 99, 61–97. https://doi.org/10.1016/j.earscirev.2009.12.001.

McGowan, H.A., Kamber, B., McTainsh, G.H., Marx, S.K., 2005. High resolution provenancing of long travelled dust deposited on the Southern Alps, New Zealand. Geomorphology 69, 208–221. https://doi.org/10.1016/j.geomorph.2005.01.005.

Moreno, T., Querol, X., Castillo, S., Alastuey, A., Cuevas, E., Herrmann, L., Mounkaila, M., Elvira, J., Gibbons, W., 2006. Geochemical variations in aeolian mineral particles from the Sahara-Sahel Dust Corridor. Chemosphere 65, 261–270.

Muhs, D.R., Benedict, J.B., 2006. Eolian additions to late Quaternary alpine soils, Indian Peaks Wilderness Area, Colorado Front Range. Arct. Antarct. Alp. Res. 38, 120–130.

Munroe, J.S., 2014. Investigating the Directionality of Eolian Dust Delivery to the Alpine Zone of the Uinta Mountains, Utah, USA. Presented at the 2014 GSA Annual Meeting in Vancouver, British Columbia, p. 36.

Munroe, J.S., 2007. Properties of alpine soils associated with well-developed sorted polygons in the Uinta Mountains, Utah. USA. Arct. Antarct. Alp. Res. 39, 578–591.

Munroe, J.S., 2005. Glacial geology of the northern Uinta Mountains, in: Dehler, C.M., Pederson, J.L., Sprinkel, D.A., Kowallis, B.J. (Eds.), Uinta Mountain Geology. Utah Geological Survey, pp. 215–234.

Munroe, J.S., O'Keefe, S.S., Quackenbush, P.J., 2015. Eolian deposition in the alpine zone of the Uinta Mountains, Utah, USA. Catena 124, 119–129.

Munroe, J.S., Laabs, B.J.C., 2009. Glacial Geologic Map of the Uinta Mountains Area, Utah and Wyoming. Utah Geological Survey Miscellaneous Publication 09-4DM.

Munroe, J.S., Norris, E.D., Carling, G.T., Beard, B.L., Satkoski, A.M., Liu, L., 2019. Isotope fingerprinting reveals western North American sources of modern dust in the Uinta Mountains, Utah, USA. Aeolian Res. 38, 39–47.

National Research Council, 2001. Basic Research Opportunities in Earth Science. The National Academies Press, Washington, DC. https://doi.org/10.17226/9981.

Neff, J.C., Ballantyne, A.P., Farmer, G.L., Mahowald, N.M., Conroy, J.L., Landry, C.C., Overpeck, J.T., Painter, T.H., Lawrence, C.R., Reynolds, R.L., 2008. Increasing eolian dust deposition in the western United States linked to human activity. Nat. Geosci. 1, 189–195. https://doi.org/10.1038/ngeo133.

Okin, G.S., Mahowald, N., Chadwick, O.A., Artaxo, P., 2004. Impact of desert dust on the biogeochemistry of phosphorus in terrestrial ecosystems. Global Biogeochem. Cycles 18. https://doi.org/10.1029/2003GB002145.

PRISM Climate Group, Oregon State U [WWW Document], n.d. URL https://prism.oregonstate.edu/ (accessed 6.16.20).

Reheis, M.C., 1999. Dust deposition and its effect on soils; a progress report. U.S.Geological Survey Professional Paper 121–131.

Reheis, M.C., Budahn, J.R., Lamothe, P.J., 2002. Geochemical evidence for diversity of dust sources in the southwestern United States. Geochim. Cosmochim. Acta 66, 1569–1587.

Reheis, M.C., Kihl, R., 1995. Dust deposition in southern Nevada and California, 1984–1989: Relations to climate, source area, and source lithology. J. Geophys. Res. 100 (D5), 8893. https://doi.org/10.1029/94JD03245.

Routson, C.C., Arcusa, S.H., McKay, N.P., Overpeck, J.T., 2019. A 4,500-year-long record of southern rocky mountain dust deposition. Geophys. Res. Lett. 46, 8281–8288. https://doi.org/10.1029/2019GL083255.

Routson, C.C., Overpeck, J.T., Woodhouse, C.A., Kenney, W.F., 2016. Three millennia of southwestern North American dustiness and future implications. PLoS One 11, e0149573.

Sears, J., Graff, P., Holden, G., 1982. Tectonic evolution of lower Proterozoic rocks, Uinta Mountains, Utah and Colorado. Geol. Soc. Am. Bull. 93, 990–997.

Soil Survey Staff, 2014. Keys to soil taxonomy. United States Department of Agriculture and Natural Resources Conservation Service 12, 372.

Sow, M., Goossens, D., Rajot, J.L., 2006. Calibration of the MDCO dust collector and of four versions of the inverted frisbee dust deposition sampler. Geomorphology 82, 360–375. https://doi.org/10.1016/j.geomorph.2006.05.013.

Thorn, C.E., Darmody, R.G., 1980. Contemporary eolian sediments in alpine zone, Colorado Front Range. Phys. Geogr. 1, 162–171.

Wesely, M., Hicks, B., 2000. A review of the current status of knowledge on dry deposition. Atmos. Environ. 34, 2261–2282.

Yaalon, D.H., Ganor, E., 1973. The influence of dust on soils during the Quaternary. Soil Sci. 116, 146–155.

Yang, F., Zhang, G.-L., Sauer, D., Yang, F., Yang, R.-M., Liu, F., Song, X.-D., Zhao, Y.-G., Li, D.-C., Yang, J.-L., 2020. The geomorphology–sediment distribution–soil formation nexus on the northeastern Qinghai-Tibetan Plateau: Implications for landscape evolution. Geomorphology 354, 107040.

Yang, F., Zhang, G.-L., Yang, F., Yang, R.-M., 2016. Pedogenetic interpretations of particle-size distribution curves for an alpine environment. Geoderma 282, 9–15. https://doi.org/10.1016/j.geoderma.2016.07.003.

Zhang, Z., Goldstein, H.L., Reynolds, R.L., Hu, Y., Wang, X., Zhu, M., 2018. Phosphorus speciation and solubility in aeolian dust deposited in the interior American West. Environ. Sci. Technol. 52, 2658–2667.

Zhao, W., Sun, Y., Balsam, W., Lu, H., Liu, L., Chen, J., Ji, J., 2014. Hf-Nd isotopic variability in mineral dust from Chinese and Mongolian deserts: implications for sources and dispersal. Sci. Rep. 4, 5837.